*Journal of The Electrochemical Society*, 2021 **168** 120501

# Novel Method for Monitoring the Electrochemical Capacitance by In Situ Impedance Spectroscopy as Indicator for Particle Cracking of Nickel-Rich NCMs: Part II. Effect of Oxygen Release Dependent on Particle Morphology

**Stefan Oswald,[*,z] Daniel Pritzl, Morten Wetjen, and Hubert A. Gasteiger[**]**

*Chair of Technical Electrochemistry, Department of Chemistry and Catalysis Research Center, Technical University of Munich, D-85748 Garching, Germany*

Nickel-rich NCMs ($LiMO_2$, with M = Ni, Co, and Mn) are increasingly commercialized as cathode active materials for lithium-ion batteries due to their high specific capacity. However, the available capacity is limited due to their structural instability at high state of charge, causing the formation of a resistive surface layer upon release of lattice oxygen, observed at different upper cutoff potentials depending on the NCM composition. To understand the impact of this instability, the correlation of oxygen release, capacity fading, and particle cracking was investigated as a function of state of charge for three nickel-rich NCMs, differing either in composition (i.e., in transition metal ratio) or in morphology (i.e., in primary crystallite size). First, the onset of the release of lattice oxygen was identified by on-line electrochemical mass spectrometry (OEMS). In electrochemical cycling experiments, the NCM capacitance was tracked in situ by impedance spectroscopy (EIS) using a micro-reference electrode while the upper cutoff potential was increased every third cycle stepwise from 3.9 V to 5.0 V. Hereby, the effect of the degree of delithiation on the discharge capacity and on the particle integrity (tracked via its surface area) was examined, both for poly- and single-crystalline NCMs.

 [DOI: 10.1149/1945-7111/ac3905]

Manuscript submitted September 17, 2021; revised manuscript received October 23, 2021. Published December 16, 2021.

The demand for nickel-rich layered lithium nickel cobalt manganese oxides (NCMs, $Li_{1+\delta}Ni_xCo_yMn_zO_2$, $x+y+z+\delta = 1$, and $0 < \delta < 0.01$) as attractive cathode active materials (CAMs) for lithium-ion batteries is constantly growing, owed to their high theoretical specific capacity of ~275 $mAh/g_{NCM}$.[1,2] As the material is required to endure thousands of charge/discharge cycles in applications such as electric vehicles or portable electronics, the used capacity of nickel-rich NCMs, easily controlled by the applied upper cutoff potential (typically set between 4.2 V and 4.4 V in graphite/NCM full-cells, depending on the NCM composition),[3] has to be limited to ~80–85 % of the theoretical capacity; otherwise, an accelerated capacity loss is observed during long-term cycling to higher states of charge (SOCs).[3–5]

This drawback, diminishing the practical energy density, is owed to the instability of the NCM layered structure at high degrees of delithiation, appearing beyond the H2-H3 phase transition at ~75 %SOC.[3,5–7] Above this limit, the release of lattice oxygen, detected by mass spectrometry for various NCM compositions,[3,8–10] is accompanied by the formation of a surface-near resistive oxygen-depleted layer, shown previously by microscopy (HR-TEM),[5,11–14] spectroscopy (EELS),[12] and diffraction (XRD and SAED).[12,14–16] This degradation of the surface-near structure of NCMs does not only add significant overpotentials during cycling, resulting in the loss of capacity and energy density,[3] but the released (singlet) oxygen also decomposes the electrolyte components.[17,18] In this reaction, protic species such as HF are produced,[17,18] initiating the dissolution of the transition metals from the NCM[19] and the redeposition on the anode that causes additional lithium loss in the SEI.[20] Since the phase transformation is mainly restricted to the surface-near regions of the NCM crystallites, reported to reach layer thicknesses of up to 20 nm,[3,11,14,16] the fraction of converted material, the extent of induced side reactions, and their impact on the battery performance depend directly on the specific surface area of the CAM (i.e., on the electrochemically active surface area) and, therefore, on the particle morphology of the CAM.

In part I of this study,[21] we successfully developed an in situ method for tracking the surface area of a battery electrode by its capacitance, obtained non-destructively from electrochemical impedance spectroscopy (EIS). With this novel tool, we showed that the surface area of a polycrystalline (PC) NCM622 increased continuously upon charge/discharge cycling, resulting from the crack formation of the secondary NCM agglomerates caused by the anisotropic change of the lattice parameters *a* and *c* upon (de)lithiation.[5,7,22–24]

Aiming to suppress the NCM surface area increase and, thereby, reduce the parasitic side reactions with the electrolyte that scale with exposed surface area, the interest for NCM particles with a monolithic structure and larger primary crystallites, so-called *single-crystalline* (SC) NCMs,[25] is growing, as they are expected to be less prone to particle cracking.[26–28] By comparing PC and SC NCM523, Li et al.[29] previously presented a significantly improved long-term cycling stability for SC NCM523 at elevated temperatures: at 40 °C, the single-crystalline NCM lasted for 300 cycles, before the capacity degraded to 90 % of its initial value, even without electrolyte additives; for the polycrystalline NCM, however, the same state of health was reached already after 150 cycles.[29] According to the study of Harlow et al., battery cells (using a similar SC NCM523 material) could deliver more than 1000 charge/discharge cycles at 40 °C, and even up to 10,000 cycles at 20 °C, before 90 % of the initial capacity was reached.[30] If it were possible to show that the surface area of SC NCMs was maintained upon cycling, the improved performance of SC NCMs[27,29] could be clearly assigned to the stability of their morphology and, therefore, to their ability to retain a low exposed surface area over the course of cycling.

In this paper, the correlation of lattice oxygen release, capacity fading, and particle cracking is investigated as a function of the state of charge for three nickel-rich NCMs, differing either in composition (i.e., in transition metal ratio: nickel content of 60 % vs. 85 %) or in morphology (i.e., in primary crystallite size: PC vs. SC). First, the onset of the release of lattice oxygen is identified by on-line electrochemical mass spectrometry (OEMS). In electrochemical

*Electrochemical Society Student Member.
**Electrochemical Society Fellow.
[z]E-mail: Stefan.Oswald@tum.de

cycling experiments, the NCM electrode capacitance is tracked in situ by impedance spectroscopy (EIS) using a micro-reference electrode (μ-RE) while the upper cutoff potential is increased every third cycle stepwise from 3.9 V to 5.0 V. Hereby, the effect of a high degree of delithiation on the discharge capacity as well as on the particle integrity, tracked by the NCM specific surface area via Kr-BET, is illuminated, both for poly- and single-crystalline NCMs. As the two NCM morphologies exhibit an entirely different integrity of the CAM particles at high state of charge, the underlying mechanisms causing the surface area increase are discussed. From the detected amounts of evolved gases as well as from the evolution of the specific surface areas of the CAMs, the thickness of the oxygen-depleted surface layer is estimated for each material.

## Experimental

***Scanning electron microscopy.***—The morphology of the cathode active material powders was investigated via top-view scanning electron microscopy (SEM) using a tabletop microscope (JCM-6000, JEOL, Japan) in secondary electron mode and applying an acceleration voltage of 15 kV.

***Electrode preparation.***—For cell cycling, NCM electrodes were prepared from three NCM powders (as presented in the SEM pictures of Fig. 2): polycrystalline NCM622 referred to as *PC-60* ($Li_{1.01}(Ni_{0.6}Co_{0.2}Mn_{0.2})_{0.99}O_2$, 0.32 $m^2_{BET}/g_{NCM}$ measured by Kr-BET), polycrystalline NCM851005 referred to as *PC-85* ($Li_{1.01}(Ni_{0.85}Co_{0.10}Mn_{0.05})_{0.99}O_2$, 0.27 $m^2_{BET}/g_{NCM}$), and single-crystalline NCM851005 referred to as *SC-85* ($Li_{1.01}(Ni_{0.85}Co_{0.10}Mn_{0.05})_{0.99}O_2$, 0.51 $m^2_{BET}/g_{NCM}$); all CAMs were received from BASF SE, Germany. The three NCM powders were each mixed at a mass ratio of 90:8:2 with vapor-grown carbon fibers (VGCF-H, 12.4 $m^2_{BET}/g_{VGCF}$, Showa Denko, Japan) and polyvinylidene difluoride (PVDF, Kynar HSV 900, Arkema, France) as well as N-methyl-2-pyrrolidone (NMP, anhydrous, Sigma Aldrich, Germany) in a planetary mixer (Thinky Corp., USA) for 17 min, using a four-step sequential mixing procedure.

For on-line electrochemical mass spectrometry (OEMS) measurements, the slurries (with a solid content of 80 wt%) were coated on a stainless-steel mesh (316 grade, 26 μm aperture, 25 μm wire diameter, The Mesh Company, UK) with a doctor blade using an automatic coater (RK PrintCoat Instruments, United Kingdom). The electrode sheets were then dried in a convection oven at 50 °C for 5 h before electrodes with a diameter of 14 mm were punched out, having a loading of 8.0 ± 2.0 $mg_{NCM}/cm^2$; this corresponds to a theoretical areal capacity of 2.2 ± 0.6 $mAh/cm^2$. For the counter electrodes, LFP electrodes with a diameter of 15 mm were punched out from commercially available LFP electrode sheets (LFP on aluminum, 3.5 $mAh/cm^2$, Custom Cells, Germany).

For the cycling experiments in Swagelok T-cells, the slurries (with a solid content of 63 wt%) were coated onto the rough side of an aluminum foil (18 μm, MTI, USA) with a box-type coating bar (Erichsen, Germany) using the automated coater. All electrode sheets were then dried in a convection oven at 50 °C for 5 h before electrodes with a diameter of 10.95 mm were punched out, having a loading of 8.7 ± 1.0 $mg_{NCM}/cm^2$; this corresponds to a theoretical areal capacity of 2.4 ± 0.3 $mAh/cm^2$. For the counter electrodes, LTO electrodes with a diameter of 10.95 mm were punched out from commercially available LTO electrode sheets (LTO on aluminum, 3.5 $mAh/cm^2$, Custom Cells, Germany).

To avoid any cracking of the NCM particles during electrode preparation, the NCM electrodes were not compressed or calendered. They were dried in a Büchi oven at 120 °C under dynamic vacuum for at least 6 h and then transferred without exposure to air to an argon-filled glove box (<1 ppm $O_2$ and $H_2O$, MBraun, Germany), where all cells were assembled.

***On-line electrochemical mass spectrometry.***—In preparation of the on-line electrochemical mass spectrometry (OEMS) experiments, the capacitively oversized LFP electrodes (15 mm, 3.5 $mAh/cm^2$) were pre-delithiated in coin cells (Hohsen, Japan) using two glass fiber separators, one H2013 polyolefin separator (Celgard, USA) facing the LFP electrode, and 100 μl of LP57 electrolyte (1 M $LiPF_6$ in EC:EMC 3:7 w/w, <20 ppm $H_2O$, BASF, Germany). For this, they were delithiated against metallic lithium (450 μm thick and 15 mm in diameter, Rockwood Lithium, USA) to ∼90 % SOC at a specific current of 30 $mA/g_{LFP}$ for 4.5 h, after having performed one full formation cycle at 30 $mA/g_{LFP}$ between 3.0 V and 4.0 V vs. $Li^+/Li$. After pre-delithiation, the LFP electrodes were harvested from the cells and used without washing as the counter electrode in the OEMS cells for the gas evolution experiments. The pre-delithiated, capacitively oversized LFP electrodes are used because they: i) provide a stable potential of ∼3.45 V vs. $Li^+/Li$ over a wide SOC window (3.40 V used at 90 %SOC for the end of lithiation), ii) provide a sufficiently large capacity to take up the lithium from the investigated NCM working electrodes, and iii) exhibit no gas evolution due to the absence of electrolyte decomposition reactions at their operating potential (as compared to typical anodes such as lithium metal or graphite forming an SEI including gas evolution[3,20,31]).

For the OEMS experiments, a pre-delithiated LFP counter electrode was placed on the bottom of the custom-made OEMS cell hardware, then covered by two H2013 polyolefin separators (24 mm, Celgard, USA) that were wetted with 100 μl of LP57 electrolyte (1 M $LiPF_6$ in EC:EMC 3:7 w/w, <20 ppm $H_2O$, BASF, Germany); finally, an NCM electrode was placed on top of the stack. The electrode stack was then compressed by a spring in the sealed OEMS cell. The assembled cells were positioned in a climate chamber (CTS, Germany) at 25 °C and connected to a potentiostat (SP-300, BioLogic, France) and the mass spectrometer system (HiQuad QMH 400–1, Pfeiffer Vacuum, Germany), which has been described in detail elsewhere.[32]

The cells were held at OCV for 4 h before they were charged in constant-current mode (CC) to 5.0 V vs. $Li^+/Li$ (corresponding to 1.6 V vs. the pre-delithiated, capacitively oversized LFP counter electrode) at a *C*-rate of *C*/15 (referenced to the theoretical capacities of 276.5 $mAh/g_{NCM}$ for PC-60 and of 275.0 $mAh/g_{NCM}$ for PC-85 and SC-85). The traced mass signals were first normalized to the ion current of the $^{36}Ar$ isotope to correct for fluctuations of pressure and temperature, and then the signals for $O_2$ and $CO_2$ were converted to concentrations using a calibration gas (argon with 2000 ppm of $H_2$, $O_2$, $C_2H_4$, and $CO_2$ each, Westfalen, Germany) and considering a cell volume of ∼11 $cm^3$. For details on the calibration procedure, see Tsiouvaras et al.[32]

***T-cell assembly.***—In preparation of the cycling experiments in Swagelok T-cells (adapted and reprinted here from part I of this study[21]), capacitively oversized LTO electrodes (3.5 $mAh/cm^2$) were pre-lithiated to ∼10 %SOC in spring-compressed T-cells with two glass fiber separators that were wetted with 60 μl of LP57 (1 M $LiPF_6$ in EC:EMC 3:7 w/w, <20 ppm $H_2O$, BASF, Germany) and a metallic lithium counter electrode (450 μm thick and 11 mm in diameter, Rockwood Lithium, USA). This was done at a specific current of 30 $mA/g_{LTO}$ for 0.5 h, after having performed one full formation cycle at 30 $mA/g_{LTO}$ between 1.2 V and 2.0 V vs. $Li^+/Li$. After pre-lithiation, the LTO electrodes were harvested from the cells. They were then used without washing as the counter electrode in the pseudo full-cells for the electrochemical cycling tests; note that pseudo full-cell here refers to a cell with a given working electrode (NCM electrodes in this work) and a capacitively oversized, pre-lithiated LTO electrode. The pre-lithiated, capacitively oversized LTO counter electrodes are used because they provide: i) a stable half-cell potential of 1.55 V vs. $Li^+/Li$ over a wide SOC window, ii) a sufficiently large capacity to take up the lithium from the investigated NCM working electrodes, and iii) a sufficient excess of lithium to compensate for any lithium consumed by side reactions during cycling, so that the NCM working electrode can be fully lithiated for the EIS measurements that are being conducted in blocking conditions (see below).

For the electrochemical cycling tests, spring-compressed T-cells with capacitively oversized pre-lithiated LTO as the counter electrode and the different NCM-based cathodes (with PC-60, PC-85, or SC-85) as working electrodes were assembled using two glass fiber separators and 60 µl of LP57. Between the two separators, a micro-reference electrode (µ-RE) was inserted, namely a gold-wire reference electrode (GWRE) based on the setup described by Solchenbach et al.[33] The GWRE was lithiated in situ at 150 nA over 1 h from the LTO counter electrode before cycling, which establishes a constant GWRE potential of 0.31 V vs. $Li^+/Li$[33] that remained stable for more than 800 h (note that the GWRE lithiation charge of ∼0.15 µAh is negligible compared to the capacity of the counter electrode). For details about the cell setup and the preparation of the gold wire, please refer to the original publication.[33]

To record the potential curves of the first charge for the three NCMs (shown in the appendix), spring-compressed Swagelok T-cells with lithium metal as the reference and counter electrode (so-called *half-cells*) and working electrodes based on PC-60, PC-85, or SC-85 were assembled using three glass fiber separators (two between working and counter electrode and one on the lithium metal reference electrode) and 90 µl of LP57 electrolyte.

***Impedance spectroscopy.***—All electrochemical impedance spectra were included directly into the cycling procedure of a multi-channel potentiostat VMP3 (BioLogic, France) and recorded in a climate chamber (Binder, Germany) at 25 °C in potentiostatic mode (PEIS), with an amplitude of 15 mV for 8 points per decade from 100 kHz to 100 mHz, including a data point at a frequency of 180 mHz. This results in an acquisition time of ∼10 min per PEIS. Each EIS spectrum consists of a full-cell spectrum (between working and counter electrode) and, by using a µ-RE (i.e., the GWRE), also of the half-cell spectrum (i.e., between the working electrode and the µ-RE).

***T-cell testing.***—All electrochemical cycling tests including the PEIS were performed in a climate chamber (Binder, Germany) at 25 °C, using a multi-channel potentiostat (VMP3, Biologic, France). Before cell cycling, the GWRE was lithiated using the pre-lithiated, capacitively oversized LTO counter electrode (see above). To acquire EIS spectra under blocking conditions, characterized by a semi-infinite charge-transfer resistance, the NCM working electrode is cycled to the fully discharged state (corresponding to ∼5 %SOC due to the irreversible capacity of the NCM materials in the first cycle) at a potential of 2.55 V vs. $Li^+/Li$, i.e., to full lithiation of the NCM working electrodes, where the working electrode potential was then held for 1 h prior to taking EIS spectra. The long-term cycling procedure is shown exemplarily for a PC-85 working electrode in Fig. 1: it was initiated by an OCV phase of 10 h, during which a PEIS was taken every 1 h (red open circles in Fig. 1). Then, in order to determine the electrode capacitance for the *pristine* NCM, the NCM working electrode was discharged to the lower cutoff potential of 2.55 V vs. $Li^+/Li$ at a specific current of 18.4 mA/$g_{NCM}$ for PC-60 and 21.4 mA/$g_{NCM}$ for PC-85 and SC-85 (both corresponding to ∼*C*/10 when referenced to the specific capacity obtained for an upper cathode potential of 4.2 V vs. $Li^+/Li$) in CC mode (orange line in Fig. 1), where a constant voltage (CV) hold of 1 h was performed, followed by a PEIS. During *conditioning* (black line in Fig. 1), the electrodes were charged at *C*/10 in CC mode for 1 h, then discharged to the lower cutoff potential of 2.55 V vs. $Li^+/Li$ at *C*/10 in CC mode, where a CV hold of 1 h was performed, followed by a PEIS (marked by the #0 point in Figs. 1 and 4). Since nickel-rich CAMs are commonly slightly overlithiated (by up to 1 %) in the synthesis process, the conditioning step was included in the procedure to ensure comparable impedance spectra for each cycle, namely by assuring that similar SOCs are obtained by the potential hold of 1 h at 2.55 V vs. $Li^+/Li$, especially when comparing different NCM active materials.

For the subsequent *cycling* (blue lines in Fig. 1), three charge/discharge cycles were executed, with a charge to the initial upper cutoff potential of the NCM electrode of 3.9 V vs. $Li^+/Li$ at *C*/10 with a CV hold until the current dropped to below 0.1 mA (∼*C*/20, CCCV mode), and with a discharge to the lower cutoff potential of 2.55 V vs. $Li^+/Li$ at *C*/10 with a final CV hold of 1 h before a PEIS was recorded (marked by the #1, #2, and #3 points in Figs. 1 and 4). This set of three cycles was then repeated while increasing the upper cutoff potential (of the cell and, therefore, for the NCM electrode) by 100 mV for each set after every third cycle, finishing with three cycles to 5.0 V vs. $Li^+/Li$ (corresponding to cycle #34, #35, and #36). The impedance spectra taken in blocking conditions are numbered by the full cycles the cell had performed up to that point (e.g., #6 after the three cycles to 4.0 V vs. $Li^+/Li$). For the surface area determination by Kr-BET, additional cells with PC-85 electrodes were stopped after cycle #9 and cycle #30, corresponding to charge/discharge cycling up to 4.1 V and 4.8 V vs. $Li^+/Li$, respectively.

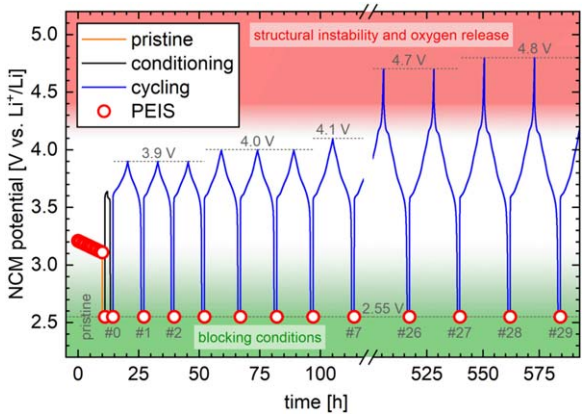


**Figure 1.** Cycling procedure shown exemplarily for a PC-85 working electrode in a pseudo full-cell with a pre-lithiated, capacitively oversized LTO counter electrode and a gold-wire reference electrode, whereby all potentials are shown vs. $Li^+/Li$, based on a potential of 1.55 V vs. $Li^+/Li$ of the LTO counter electrode (analogous procedures were used for PC-60 and SC-85 working electrodes). The long-term cycling procedure consists of an initial OCV phase of 10 h, the discharge to blocking conditions of the pristine electrode (orange line), a conditioning step (black line), and the cycling to an upper cutoff potential which increases every three cycles from initially 3.9 V to 5.0 V vs. $Li^+/Li$ (blue line), with the intermittent acquisition of EIS spectra (red circles) under blocking conditions at the points marked with #0, #1, etc.

To allow for the assignment of the applied potential to a state of charge (or degree of delithiation) for each of the three NCMs, the NCM electrodes assembled in half-cells were charged against the potential of a metallic lithium reference electrode in constant-current mode (CC) to 5.0 V vs. $Li^+/Li$ at a specific current of 18.4 mA/$g_{NCM}$ (corresponding to a *C*-rate of *C*/15 when referenced to the theoretical capacities of 276.5 mAh/$g_{NCM}$ for PC-60 and of 275.0 mAh/$g_{NCM}$ for PC-85 and SC-85), using a battery cycler (Series 4000, Maccor, USA).

***Cell disassembly.***—After cycling, the electrodes were harvested from the pseudo full-cells under inert atmosphere to determine their specific surface area by Kr-BET. Any residue of the conductive salt was removed from the electrodes in a three-step sequential washing procedure: first, they were washed for 5 min in 5 ml EC:EMC 3:7 w/w (Gelon Lib, China), followed by a soaking step of 24 h in 1 ml DMC (anhydrous, ⩾99 %, Sigma Aldrich, USA) and, finally, a washing step of 5 min in 5 ml DMC.

***Surface area analysis.***—The surface area of the NCM powders as well as of the pristine and of the harvested and washed PC-85 electrodes was determined by krypton gas physisorption measurements at 77 K, as previously presented by Friedrich et al. and Oswald et al.,[14,21] measuring at 13 points between

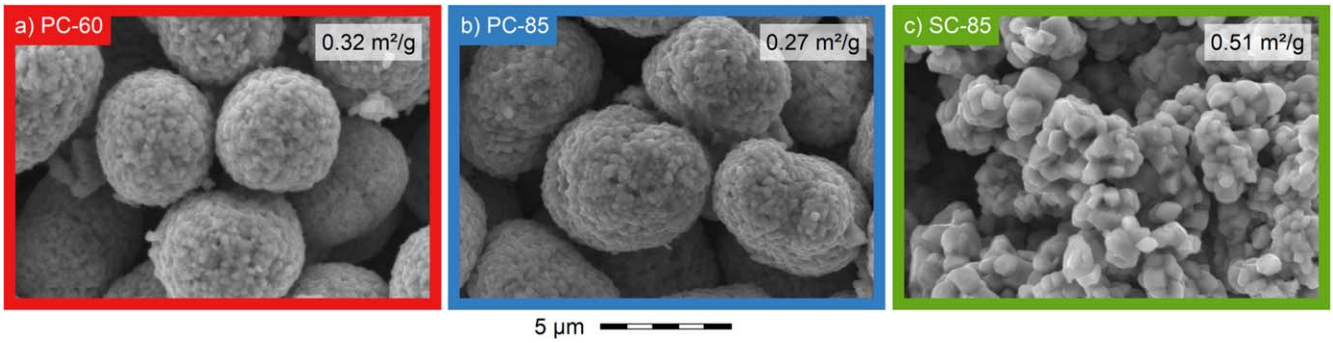


**Figure 2.** Visual investigation of the particle morphology of the three pristine NCM powders by top-view SEM in secondary electron mode at 15 kV. **a)** Polycrystalline NCM622 (PC-60). **b)** Polycrystalline NCM851005 (PC-85). **c)** Single-crystalline NCM851005 (SC-85). The specific surface area obtained by Kr-BET is displayed for each material in the respective panel.

$0.01 \leqslant p/p_0 \leqslant 0.30$, using an autosorb iQ (Quantachrome Instruments, USA). Comparative $N_2$-BET measurements for the pristine materials (VGCF and NCM powders) are within ±10 % of the specific surface areas obtained by krypton physisorption (also referred to as Kr-BET). The advantage of the measurement with krypton is a superior sensitivity of this method, since only ca. $1/100^{th}$ of the total surface area is required for the physisorption measurements, so that Kr-BET areas can be obtained electrodes with a diameter of 11 mm, whereby an approximately 100-fold larger electrode area would be required for meaningful $N_2$-BET measurements. Prior to Kr-BET measurements, both powder samples as well as samples of pristine or harvested and washed electrodes were dried at 120 °C under vacuum for 6 h.

## Results and Discussion

***Visual investigation of pristine NCM powders.—***To be able to understand and interpret the results of their later electrochemical characterization, at first, the morphology of the three NCM cathode active material (CAM) powders is examined, based on the representative SEM pictures depicted in Fig. 2. The polycrystalline (PC) NCM622 powder (PC-60, labeled in red color), as shown in Fig. 2a, consists of spherical secondary agglomerates (∼5–10 µm in diameter, obtained by a visual investigation) with a relatively narrow particle size distribution (as one would expect for CAM powders synthesized in a batch process). The secondary particles themselves are comprised of numerous primary crystallites (∼0.1–0.5 µm). As shown in Fig. 2b, the polycrystalline NCM851005 powder (PC-85, labeled in blue color), which has an increased nickel content of 85 % as compared to PC-60 with 60 %, has a similar particle morphology. In contrast to the polycrystalline materials, the single-crystalline NCM851005 (SC-85, labeled in green color), shown in Fig. 2c, has the same transition metal composition as PC-85 but consists of much larger primary crystallites (∼0.5–2.0 µm), which are randomly agglomerated or sintered, without having a well-defined secondary structure as compared to the polycrystalline CAMs.

Upon (de)lithiation, the NCM materials experience a significant unit cell volume change,[7,22] what results in stress and strain throughout the secondary particles, leading to cracking of the agglomerates and a surface area increase of the NCM particles.[21] Since the absolute strain would be larger for bigger particles, one could expect different behavior of smaller and larger particles contributing to the measured surface area increase during the electrochemical investigation. However, due to the relatively narrow secondary particle size distribution of the two PC materials as well as due to the similar particle size and, therefore, specific surface area, any possible influence of different particle sizes on the evolution of the morphology of the materials can be excluded. Furthermore, as the ink preparation did not include any harsh mixing procedures like ball-milling (a planetary mixer was used here), and as the electrodes were not compressed or calendered, the particle morphology of the powders was not altered during the electrode preparation. For these reasons, a comparison of the two polycrystalline NCMs (PC-60 and PC-85) allows to examine the effect of the composition (i.e., the transition metal ratio and the nickel content) on the gas evolution and the increase in surface area. In contrast, the investigation of the polycrystalline and single-crystalline nickel-rich materials that have the same composition (PC-85 and SC-85) allows to elucidate the effect of NCM particle morphology on the surface area increase upon cycling and on the associated gas evolution. Additionally, a comparison of these two materials should make it possible to discriminate between the particle cracking of the primary and of the secondary NCM particles, as SC-85 consists only of primary crystallites without a well-defined secondary structure, so that a surface area increase would only occur upon cracking of the primary particles.

***Oxygen release at high state of charge.—***As morphological changes of NCM particles cannot only be caused through the repeated unit cell volume change upon long-term charge/discharge cycling (see part I of this study[21]), but may also be caused by the release of lattice oxygen at high state of charge[3] (SOC, note that the SOC is defined in this work as the degree of delithiation $x$ in $Li_{1-x}MO_2$), we next investigate the onset and the amount of $O_2$ and $CO_2$ gas evolution of the three NCMs by on-line electrochemical mass spectrometry (OEMS) as a function of the degree of delithiation (note that the evolution of CO was below 1 $\mu mol_{CO}/g_{NCM}$ and will thus not be discussed here). In Fig. 3a, the potential profiles of the first charge of the three NCMs to 5.0 V vs. $Li^+/Li$ in an OEMS cell are depicted as a function of time and SOC, respectively. The voltage curve of PC-60 (red) appears above the ones of the nickel-rich equivalents PC-85 (blue) and SC-85 (green); therefore, more capacity is extracted at the same potential for the nickel-rich materials—or, in other words, a lower cutoff potential is required to reach the same SOC. Since PC-85 and SC-85 have the same composition, the voltage profiles are essentially identical, especially in the range between 50 %SOC and 90 %SOC, which is relevant for this work. As the nickel content of PC-85 and SC-85 comes relatively close to the one of a pure layered lithium nickel oxide (LNO, $LiNiO_2$), a first evidence of a plateau at 4.2 V vs. $Li^+/Li$ of the potential curve can be seen, indicating the H2-H3 phase transition,[5–7] which is reported to be the cause for the release of lattice oxygen.[3]

The onset and the amount of molecular oxygen ($O_2$) released from the NCM (quantified via mass spectrometry by the mass-over-charge ratio $m/z = 32$) is analyzed from Fig. 3b. Upon charging of the NCMs, the oxygen levels remain zero up to ∼80 %SOC, at which point all three materials start to evolve oxygen almost independently of nickel content, as stated by Jung et al. in previous reports.[3,9] The onset of the oxygen evolution for PC-60 seems to be shifted to lower SOCs by ∼5–10 %SOC as compared to PC-85 and SC-85; this observation will be subject of future studies. Nevertheless, most of the oxygen is released above ∼80 %SOC

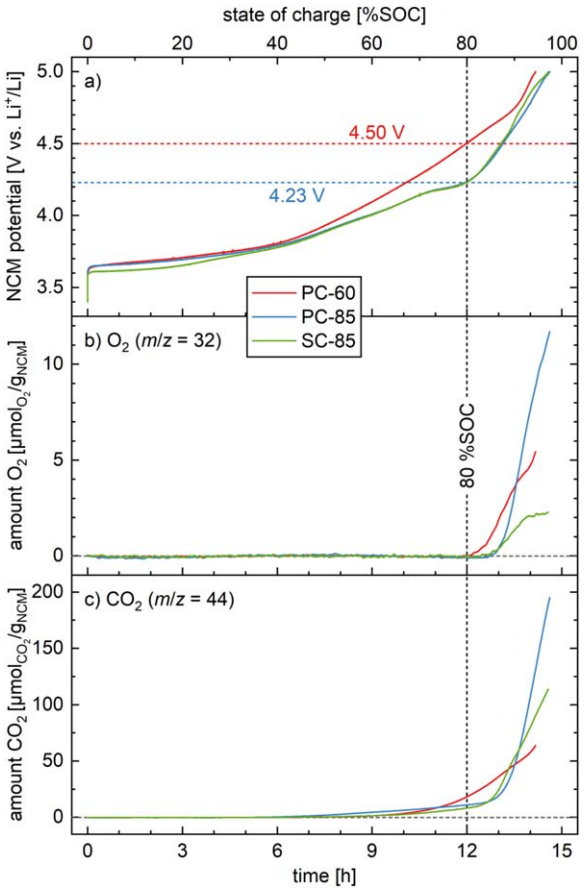


**Figure 3.** Electrochemical data and gas evolution of OEMS cells assembled with PC-60 (red), PC-85 (blue), and SC-85 (green) as working electrodes, using delithiated, capacitively oversized LFP as counter electrode, two Celgard H2013 separators, and 100 µl LP57 electrolyte. The cells were charged at 25 °C to 5.0 V vs. $Li^+$/Li (corresponding to a cell voltage of 1.6 V) in constant current mode at 18.4 mA/$g_{NCM}$ (corresponding to *C*/15 when referenced to ∼275 mAh/$g_{NCM}$) while the gas evolution was recorded by mass spectrometry. All data are shown as a function of both time (lower x-axis) and state of charge (referenced to ∼275 mAh/$g_{NCM}$; upper x-axis). **a)** NCM potential vs. $Li^+$/Li (calculated from the cell voltage and the potential of 3.40 V vs. $Li^+$/Li for LFP during the end of its lithiation). **b)** and **c)** Total amounts of evolved oxygen ($O_2$, mass-over-charge ratio $m/z = 32$) and carbon dioxide ($CO_2$, $m/z = 44$) in the OEMS cell, respectively, which were normalized to the NCM mass. The horizontal dashed lines mark the potential at which 80 %SOC are reached for PC-60 (red) as well as for PC-85 and SC-85 (blue).

for the two different NCM compositions, corresponding to 4.50 V vs. $Li^+$/Li for PC-60 and 4.23 V vs. $Li^+$/Li for PC-85 and SC-85. For PC-85 and SC-85, the value of ∼80 %SOC nicely coincides with the end of the plateau at 4.2 V vs. $Li^+$/Li (see intersection of the horizontal green and blue lines with the vertical dashed black line in Fig. 3a), at which point the H2-H3 phase change is completed. The amount of detected oxygen rises with increasing degree of delithiation, which indicates an increasing destabilization of the layered oxide lattice structure, causing the transformation to the oxygen-depleted surface structure. At 5.0 V vs. $Li^+$/Li, corresponding to ∼100 %SOC ideally, the total amount of oxygen from PC-60 in this experiment amounts to 5.4 µmol$_{O_2}$/$g_{NCM}$, which is approximately half the amount as compared to the value for PC-85 with 11.7 µmol$_{O_2}$/$g_{NCM}$ and approximately twice as much as compared to SC-85 with 2.5 µmol$_{O_2}$/$g_{NCM}$. Even though the evolution of oxygen almost vanishes before the upper potential limit at ∼4.8 V for the single-crystalline material (see green line in Fig. 3b), it must be noted that the release of lattice oxygen does not seem to be completed yet as the increase of $CO_2$ continues for all three NCM materials.

Due to the reaction of the (singlet) oxygen released from the NCM lattice with the electrolyte, a large fraction of it is detected as carbon dioxide ($CO_2$, $m/z = 44$), what is depicted in Fig. 3c. The $CO_2$ signal of the three NCMs remains zero until ∼40 %SOC, corresponding to ∼3.8 V vs. $Li^+$/Li for all three NCMs. This potential is sufficiently high to initiate the electrochemical oxidation of alcohols such as ethylene glycol or ethanol[8,34] and other unwanted trace impurities remaining in the electrolyte from the synthesis of the carbonate-based solvents. One product of this process are protons ($H^+$) which chemically decompose lithium carbonate ($Li_2CO_3$) that remains on the NCM particles (from the lithium excess typical for the synthesis of the active material), resulting in the formation of lithium ions, water, and carbon dioxide.[34] Furthermore, the produced water in the electrolyte reacts with the conducting salt $LiPF_6$, which again generates protons,[35] resulting in an autocatalytic cycle decomposing $Li_2CO_3$ and evolving $CO_2$.[34] Therefore, we believe that the $CO_2$ detected above ∼3.8 V vs. $Li^+$/Li and prior to the onset potential for oxygen evolution predominantly stems from the electrochemical oxidation of electrolyte impurities and the chemical decomposition of $Li_2CO_3$. Up to ∼80 %SOC (corresponding to 12 h in the experiment), 18.6 µmol$_{CO_2}$/$g_{NCM}$ of $CO_2$ were detected for PC-60, 11.2 µmol$_{CO_2}$/$g_{NCM}$ for PC-85, and 8.5 µmol$_{CO_2}$/$g_{NCM}$ for SC-85. Assuming that these amounts of $CO_2$ would indeed be due to the decomposition of $Li_2CO_3$, this would require a minimum $Li_2CO_3$ impurity level of the NCMs ranging between 0.06–0.14 wt%, which is within typical values.

At ∼80 %SOC, a sharply increasing slope of the $CO_2$ signals of PC-85 and SC-85 (corresponding to a change in $CO_2$ production rate) is observed. This SOC coincides with the $O_2$ release from the NCM lattice in the near-surface region of the NCM particles, which is why we assign most of the released $CO_2$ above ∼80 %SOC to the chemical oxidation of electrolyte.[8] At the end of charge, 64 µmol$_{CO_2}$/$g_{NCM}$ of $CO_2$ were detected for PC-60, 195 µmol$_{CO_2}$/$g_{NCM}$ for PC-85, and 114 µmol$_{CO_2}$/$g_{NCM}$ for SC-85. The cause for the differing gas amount of the three NCMs will be discussed in a later section, where we estimate the thickness of the oxygen-depleted surface layer.

In summary, the release of reactive lattice oxygen from the surface-near regions of the NCM particles accompanied by a $CO_2$ evolution is almost independent of nickel content and occurs at an SOC of ∼80 %; at this SOC, however, the NCM cathode potential is lower for a nickel-rich NCM.

***Charge/discharge cycling with increasing upper cutoff potential.—***In the following, the effect of the state of charge (SOC) on the discharge capacity and on the morphology of the NCM active materials is investigated. For this, the upper cutoff potential of the NCM working electrode is increased stepwise by 0.1 V every third cycle, inducing structural and morphological changes which are illuminated through the measurement of the electrode capacitance in the discharged state (i.e., under blocking conditions). Aiming to track the behavior of fully intact NCM particles, electrodes that were not compressed or calendered were cycled, as the mechanical compression could lead to the partial breakage of the secondary agglomerates already before the measurement.[21] To ensure electronic connection throughout the entire electrode even without compression or calendering, vapor-grown carbon fibers with a length of 15 µm were used as conductive additive.

The specific discharge capacity of all three NCMs, depicted in Fig. 4a, increases after each set of three cycles, i.e., with each increase in the upper cutoff potential of the NCM working electrode. For lower cutoff potentials, the delivered capacity is higher for the nickel-rich materials PC-85 and SC-85 as compared to PC-60, consistent with the NCM charge curves shown in Fig. 3a and in Fig. A·2. When cycling to upper cutoff potentials that are below the onset of lattice oxygen release at ∼80 %SOC (marked by a vertical

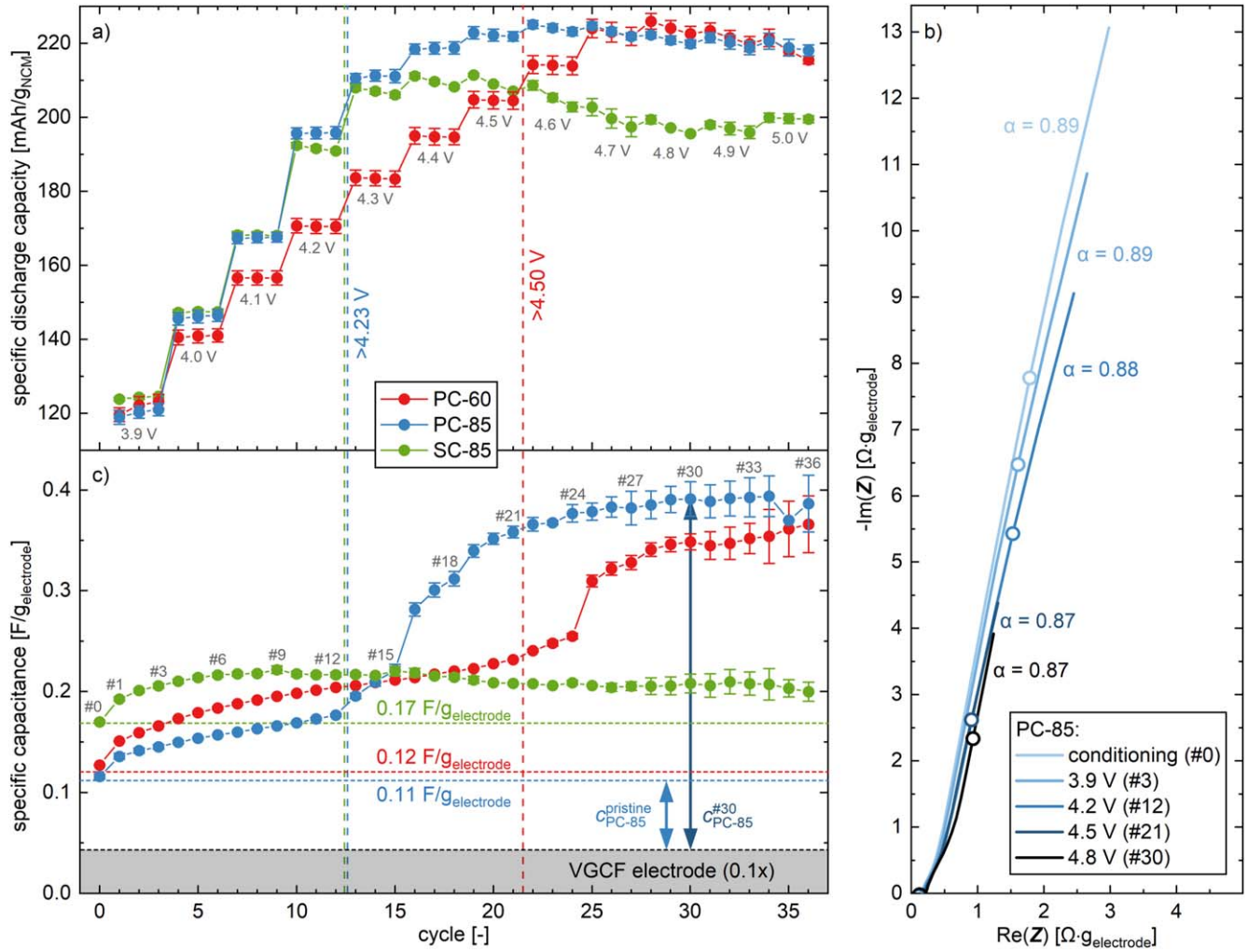


**Figure 4.** Electrochemical cycling data of PC-60 (red), PC-85 (blue), and SC-85 (green) as working electrodes in pseudo full-cells with a μ-RE (i.e., a GWRE), using pre-lithiated, capacitively oversized LTO as the counter electrode, two glass fiber separators and 60 μl LP57 electrolyte. Following the procedure depicted in Fig. 1, the cells were cycled at 25 °C to a selected upper cutoff potential of the NCM electrode that was increased every three cycles by 0.1 V starting at 3.9 V vs. $Li^+$/Li. The current applied for cell cycling was 18.4 mA/$g_{NCM}$ for PC-60 and 21.4 mA/$g_{NCM}$ for PC-85 and SC-85 (this corresponds to *C*/10 when referenced to the specific capacity obtained for an upper cathode potential of 4.2 V vs. $Li^+$/Li). Impedance spectra of the NCM working electrodes were recorded in blocking conditions after a potential hold of 1 h at 2.55 V vs. $Li^+$/Li (15 mV amplitude, from 100 kHz to 100 mHz). The vertical dashed lines mark the cycle at which ∼80 %SOC (extracted from Fig. 3) are exceeded for each of the three NCMs (4.50 V for PC-60, and 4.23 V for PC-85 and SC-85), marking the onset of the release of lattice oxygen. The specific capacitance and the specific discharge values are calculated from the mean of two nominally identical cells, with the error bars corresponding to the minimum/maximum values. **a)** Specific discharge capacity for the respective upper cutoff potential normalized to the NCM mass as a function of cycle number. **b)** Selected impedance spectra in blocking conditions of the PC-85 working electrode after the conditioning cycle (referred to as #0), after the three cycles to 3.9 V (referred to as #3), 4.2 V (#12), 4.5 V (#21), and 4.8 V (#30) (see also Fig. 1), while the respective frequency points at 180 mHz are indicated by empty circles. **c)** Specific capacitance of the NCM working electrode extracted from the imaginary impedance at 180 mHz in blocking conditions as a function of cycle number. The horizontal dashed lines indicate the pristine capacitance value of each of the three NCM working electrodes before the conditioning step (#0). The gray area marks the specific capacitance of the VGCF electrode multiplied by 0.1.

dashed line for each material), the discharge capacity stays constant during each set of three cycles. As the upper cutoff potential exceeds the onset potential for lattice oxygen release by more than ∼0.1 V, the discharge capacity starts to fade within each set of three consecutive cycles. For PC-60 (red symbols), the discharge capacity at 4.7 V decreases by 2 mAh/$g_{NCM}$ in the course of three cycles (see cycle #25 to #27) and by 4 mAh/$g_{NCM}$ at 4.8 V (see cycle #28 to #30). A similar capacity fading behavior is observed for PC-85 (blue symbols) and SC-85 (green symbols), but already starting at ∼4.2 V. Additionally, the discharge capacity fading of the SC-85 material within each set of three cycles decreases significantly above ∼4.2 V, namely by 2 mAh/$g_{NCM}$ at 4.3 V (from cycle #13 to #15) and by 4 mAh/$g_{NCM}$ at 4.5 V (from cycle #19 to #21), while no such fading is observed for these potentials for the PC-85 material. Overall, independent of the upper cutoff potential, the discharge capacity of the polycrystalline NCMs does not exceed 225 mAh/$g_{NCM}$ (or 211 mAh/$g_{NCM}$ for the single-crystalline NCM), corresponding to ∼82 %SOC. Taking into account the initial irreversible capacity of these NCMs of ∼12 mAh/$g_{NCM}$ or ∼5 %SOC (for all NCMs in cycle #0), the structural instability of the NCMs apparently limits the accessible SOC to ∼87 %SOC for the polycrystalline NCMs (or ∼81 %SOC for the single-crystalline NCM). The impact of the compositions and morphologies of the three NCMs on the here observed onset of the capacity fading as well as on the differences in (maximum) discharge capacity will be further examined when discussing Fig. 6.

To track the effect of a high SOC on the morphological stability of the three NCMs, the electrode capacitance was measured in situ from the recorded impedance spectra as a function of the upper cutoff potential. All spectra of the working electrode were collected via the μ-RE (i.e., the gold-wire reference electrode[33] (GWRE)) after each cycle in the fully discharged state at an NCM potential of

2.55 V vs. $Li^+$/Li. As the charge transfer of NCMs is impeded in the fully discharged/lithiated state, resulting in a semi-infinite value of the charge-transfer resistance (so-called *blocking conditions*), the impedance is dominated by the capacitive contribution of the electrochemical double layer at the electrode/electrolyte interface.[21,36] Assuming that the surface-area-normalized capacitance is distinct, constant, and uniformly distributed for each of the electrode components (i.e., the active material and the conductive carbon), the capacitance contribution of each of the electrode materials would be proportional to their respective surface area, an assumption that was proven by Kr-BET in part I of this study.[21] There, we had also shown that the electrode capacitance does not necessarily have to be extracted from a fit of the entire impedance spectrum, but that the impedance of the individual frequency point at 180 mHz is sufficient to accurately determine the electrode capacitance (see below).[21] For more details about the developed method and the applied analysis, please refer to the original publication.

Prior to charge/discharge cycling, it was verified that the impedance spectra of the NCM working electrodes are stable over time during the initial OCV phase of 10 h (data not shown), so that any time-dependent effects on the impedance can be excluded. Figure 4b shows five selected impedance spectra of the same PC-85 working electrode after the conditioning cycle (referred to as #0), and after the 3rd cycle at the here selected upper cutoff potentials of 3.9 V, 4.2 V, 4.5 V, and 4.8 V (referred to as #3, #12, #21, and #30, respectively). First, it is observed that blocking conditions are achieved in all instances upon the full lithiation of the NCM particles through a potential hold of 1 h at 2.55 V vs. $Li^+$/Li. The very small semicircle at high frequencies (see Fig. 4b) is due to a contact resistance at the interface between the NCM electrode and the aluminum current collector, as shown previously for uncompressed LFP,[33,37] $LiNi_{0.5}Mn_{1.5}O_4$,[38] and NCM622[21] electrodes. Similar to part I of this study, where we investigated the impedance of NCM622 electrodes under blocking conditions, the phase angle (extracted from an *R*-*Q* fit of the frequency points between 0.1 Hz and 1 Hz) of $\alpha = 0.89$ for the conditioned PC-85 electrode (see spectrum #0 in Fig. 4b) only decreases negligibly to 0.87 after the third cycle at 4.8 V (cycle #30). As the phase angle does not decrease below $\alpha = 0.85$ even at 5.0 V (data not shown), the theoretical considerations discussed in part I of this study still apply, and the electrode capacitance can be extracted from the impedance at 180 mHz with an error of less than ±1 % as compared to the value extracted from the fit.[21]

As shown in Fig. 4b, the length of the capacitive branch decreases considerably with increasing cycle number (and, therefore, with increasing upper cutoff potential), also illustrated by the decreasing value of the imaginary impedance at 180 mHz (marked by the empty circles), which decreases from 7.8 $\Omega \cdot g_{electrode}$ for the conditioned PC-85 electrode (see cycle #0) to values of 6.5 $\Omega \cdot g_{electrode}$ after 3.9 V (#3), 5.4 $\Omega \cdot g_{electrode}$ after 4.2 V (#12), 2.6 $\Omega \cdot g_{electrode}$ after 4.5 V (#21), and to 2.3 $\Omega \cdot g_{electrode}$ after 4.8 V (#30). As the imaginary impedance is inversely proportional to the capacitance of a purely capacitive circuit element, its decreasing contribution corresponds here to an increasing value of the capacitance. Quantitatively, the electrode capacitance is obtained from the imaginary part of the electrode impedance $\boldsymbol{Z}_{\omega_0}$ at the selected frequency of $f_0 = 180$ mHz (with $\omega_0 = 2 \cdot \pi \cdot f_0$) using Eq. 1, previously derived in part I of this study[21]:

$$Q \approx \frac{1}{\omega_0 \cdot (-\mathrm{Im}(\boldsymbol{Z}_{\omega_0}))} \quad [1]$$

The thus obtained capacitance values can then be normalized by the electrode mass and are depicted in units of $F/g_{electrode}$ in Fig. 4c. The pristine capacitance (shown as horizontal dashed line) is found to be 0.12 $F/g_{electrode}$ for PC-60, 0.11 $F/g_{electrode}$ for PC-85, and 0.17 $F/g_{electrode}$ for SC-85, and is essentially identical with the values obtained for the conditioned electrode (data points at cycle #0). Contained in these electrode capacitance values is the capacitance contribution from the conductive carbon and the binder (here referred to as inert components), which was identified to be 0.43 ± 0.01 $F/g_{electrode}$ for an electrode containing exclusively VGCF and PVDF (4:1 w/w).[21] As only 10 wt% of the NCM electrode consist of VGCF and PVDF, the contribution of the inert components to the NCM electrode capacitance is thus 0.043 ± 0.001 $F/g_{electrode}$ and is marked by the gray area in Fig. 4c. By subtracting this contribution of the inert components from the NCM electrode capacitance, the capacitance of the NCM only can be obtained. Exemplarily for the PC-60 working electrode, the NCM capacitance equates to 0.07 $F_{NCM}/g_{electrode}$, corresponding to 0.08 $F_{NCM}/g_{NCM}$, considering that the NCM content in the electrode is 90 wt% ($m_{NCM} = 0.9 \cdot m_{electrode}$). Analogously, values of 0.09 $F_{NCM}/g_{NCM}$ and 0.14 $F_{NCM}/g_{NCM}$ are obtained for PC-85 and SC-85, respectively.

By dividing the thus determined NCM capacitances by the specific surface areas ($S_{BET}$) of the pristine NCM powders obtained through krypton gas physisorption measurements (in the following referred to as Kr-BET), the surface-area-normalized NCM capacitances equate to 27 $\mu F_{NCM}/cm^2{}_{NCM}$ for PC-60, 29 $\mu F_{NCM}/cm^2{}_{NCM}$ for PC-85, and 28 $\mu F_{NCM}/cm^2{}_{NCM}$ for SC-85. By the same approach, a surface-area-normalized capacitance of 4.4 $\mu F_{VGCF}/cm^2{}_{VGCF}$ was determined for VGCF (12.4 $m^2/g$). Even though the NCMs show a six-fold higher areal capacitance as compared to VGCF, the results are in agreement with literature data for aqueous systems: for carbon, a typical electrode material in supercapacitors, the surface-area-normalized capacitance has been reported to be ~2–10 $\mu F/cm^2$,[39–41] while the values for metals and metals oxides are typically ~15–60 $\mu F/cm^2$.[42–46] For a Ni/NiO-based system, being rather similar in composition to the here used nickel-rich NCMs, Liu et al. found a surface-area-normalized capacitance of ~25 $\mu F/cm^2$.[43] Even though the reported values for the double-layer capacitance were measured in aqueous systems only, they are similar to the ones we have measured here in the LP57 electrolyte, likely due to similar values of the dielectric constant of water ($\varepsilon_r \approx 80$) and the here used carbonate-based solvents ($\varepsilon_r \approx 65-95$).[47] As it is assumed that the determined values of ~28 $\mu F_{NCM}/cm^2{}_{NCM}$ and 4.4 $\mu F_{VGCF}/cm^2{}_{VGCF}$ remain constant during the course of the experiment, this correlation allows for the determination of the specific surface area of the CAM powder from the measured electrochemical capacitance.

The evolution of the capacitance of the NCM electrode is depicted in Fig. 4c for the three NCMs as a function of cycle number (and, hence, of upper cutoff potential). After the conditioning step (corresponding to cycle #0), during which ~10 % of the lithium were deintercalated to ensure a similar lithium content for all subsequent impedance measurements in blocking conditions, the capacitance of the three NCMs is insignificantly higher (<6 %) as for the pristine electrodes. During the first nine full cycles (cycle #1 to #9) to relatively low upper cutoff potentials (⩽4.1 V vs. $Li^+$/Li), the electrode capacitance then increases continuously, what we assign to the repeated unit cell volume change of the NCM materials upon (de)lithiation.[7,21,22] As the crystal planes of the numerous primary crystallites are oriented arbitrarily, and as the change of the lattice parameters *a* and *c* is anisotropic, the repeated (de)lithiation induces stress and strain in the agglomerates, leading to crack formation primarily between the primary crystallites of the polycrystalline materials. The penetration of the electrolyte into the cracks is then accompanied by an increase in the NCM/electrolyte interface, which leads to the observed capacitance increase. This is observed even for the single-crystalline material that has no hierarchical secondary agglomerates, so that it is likely due to the (partial) separation of the adhered/sintered primary crystallites. After three cycles to 4.1 V, the capacitance of the PC-60 electrode has increased to 0.20 $F/g_{electrode}$, to 0.17 $F/g_{electrode}$ for PC-85, and to 0.22 $F/g_{electrode}$ for SC-85; when considering only the NCM contribution to the capacitance (i.e., in units of $F_{NCM}/g_{NCM}$, shown in Fig. A·1 in the Appendix), the NCM capacitance change between the

pristine electrodes and the electrodes after the third cycle to 4.1 V (cycle #9) is 2.0x for the PC-60, 1.8x for the PC-85, and 1.4x for the SC-85 electrodes.

The capacitance of the single-crystalline material remains at this value, even when cycled to upper cutoff potentials of 5.0 V (cycle #9 to #36 of the green curve in Figs. 4c and A·1), at which the release of lattice oxygen is known to lead to a reconstruction of the surface-near region into a rock-salt-type structure, implying the morphological stability of the (primary) single-crystalline particles even at a nearly full delithiation. In contrast, the electrode capacitance of the polycrystalline materials is increased abruptly as soon as the upper cutoff potential exceeds the onset of oxygen release (marked by the blue and red dashed vertical lines in Fig. 4c). Most of this increase is completed within nine cycles, corresponding to an additional ∼0.3 V above the onset potential of the lattice oxygen release for both polycrystalline materials. For PC-85 (blue curve), the slope of the capacitance curve starts to increase at 4.3 V vs. $Li^+$/Li (oxygen release at ∼4.23 V, see Fig. 3). When cycled to 4.4 V, a sudden jump in the capacitance is observed, which further increases during the subsequent cycles, however, then reaches a stable value of ∼0.40 $F/g_{electrode}$ during the final nine cycles (cycle #30 in Fig. 4c). A similar behavior is observed for PC-60 (red curve), however, occurring at a higher cycle number: the change in electrode capacitance increases at a potential of ∼4.5 V (oxygen release at ∼4.50 V, see Fig. 3) and an abrupt increase is observed subsequently when cycling to 4.7 V. During the final nine cycles, the capacitance of PC-60 stabilizes at a value of ∼0.35 $F/g_{electrode}$. The quantitative analysis of the NCM capacitance in contrast to the here examined electrode capacitance will be performed later when discussing Fig. 6 and Table I.

***Validation of the surface area increase by Kr-BET.***—To confirm that the shown increase in capacitance of the NCM electrodes induced by the increase of the upper cutoff potential is in fact corresponding to an increase of the specific surface area of the electrode, the Kr-BET surface area (hatched bars in Fig. 5, plotted vs. the right y-axis) is determined for PC-85 electrodes in the pristine state, for those cycled to 4.1 V vs. $Li^+$/Li, and for those cycled to 4.8 V; these are then compared to the electrode capacitance (solid bars, plotted vs. the left y-axis) at the respective point in the cycling procedure (extracted from Fig. 4c: pristine value from horizontal dashed line, #9 for 4.1 V, and #30 for 4.8 V). For this comparison, it is assumed that the contribution of VGCF and PVDF (black bars) remains constant during the experiment. This assumption is reflected in Fig. 5 by scaling the y-axes for the capacitance (left y-axis) and for the specific surface area (right y-axis) such that all values for the VGCF electrodes are at the same position for both y-axes. To obtain the contribution of the NCM only (blue bars in Fig. 5), $1/10^{th}$ of the determined values for specific capacitance and the specific surface area of the electrode containing VGCF and PVDF only (i.e., 0.1x of 0.43 $F/g_{electrode}$ and 0.1x of 7.8 $m^2/g_{electrode}$) is subtracted from the respective values obtained for the NCM electrodes, as they comprise 10 wt% of VGCF and PVDF. It is obvious that the relative contribution of NCM differs depending on the used method: for the pristine electrodes, the NCM capacitance of 0.07 $F/g_{electrode}$ contributes 61 % to the total electrode capacitance of 0.11 $F/g_{electrode}$ (see left solid bars), whereas the NCM surface area of 0.22 $m^2/g_{electrode}$ contributes only 22 % to the total electrode surface area of 1.00 $m^2/g_{electrode}$ (see left cross-hatched bars). Therefore, the contribution of the NCM to the total electrode capacitance, as depicted in Fig. 5, is six times larger than its contribution to the electrode specific surface area. This is explained by the ∼6-fold higher surface-area-normalized capacitance of NCM (28 $\mu F_{NCM}/cm^2_{NCM}$) as compared to VGCF (4.4 $\mu F_{VGCF}/cm^2_{VGCF}$), as already discussed in the previous section (listed also in the 5th row of Table I), whereas the ratio of the surface area determined by Kr-BET corresponds to the actual physical surface area, independent of the type of material. Even though the areal capacitance differs between the two electrode components, the relative increase of the contribution of the NCM only can be compared for each of the two properties.

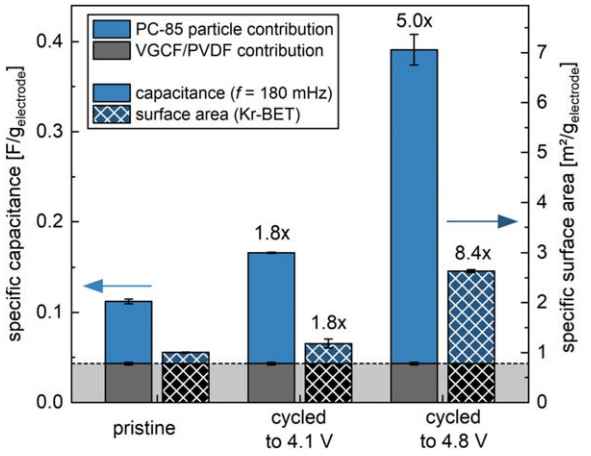


**Figure 5.** Comparison of the effect of the upper cutoff potential on the capacitance and on the Kr-BET surface area of discharged PC-85 electrodes: specific capacitance (left axis, extracted from the blue data in Fig. 4c) of pristine electrodes (corresponding to the blue horizontal dashed line and blue arrow in Fig. 4c, left-hand set of bars), after three cycles to 4.1 V vs. $Li^+$/Li (after a total of nine cycles, middle set of bars), and after three cycles to 4.8 V vs. $Li^+$/Li (after a total of 30 cycles, corresponding to the dark blue arrow in Fig. 4c, right-hand set of bars), which were obtained by using the imaginary impedance at 180 mHz according to Eq. 1 (solid bars). Specific surface area (right axis) of pristine and cycled PC-85 electrodes (cross-hatched bars) measured by Kr-BET. The contributions to capacitance and specific surface area by the PC-85 particles are colored in blue and were obtained by subtracting the weight-fraction-normalized contributions from the VGCF electrodes (colored in black). The left (capacitance) and right axis (surface area) are scaled such that the values for the VGCF electrodes are at the same position for both axes. All values are calculated from the mean of two nominally identical cells (capacitance) or two nominally identical electrodes (Kr-BET), and the error bars correspond to the minimum/maximum values. The numbers above the bars mark the increase of the NCM contributions to the electrode capacitance and specific surface area compared to the ones of the pristine electrodes.

Upon cycling, the NCM capacitance contribution to the electrode (blue solid bars) increases from 0.07 $F/g_{electrode}$ in the pristine state to 0.12 $F/g_{electrode}$ for the electrodes cycled to 4.1 V, corresponding to a change by a factor of ∼1.8x, consistent with the increase of the NCM specific surface area (blue hatched bars) by the same factor, namely from 0.22 $m^2/g_{electrode}$ to 0.40 $m^2/g_{electrode}$. This suggests a direct proportionality between capacitance and specific surface area. When cycling to 4.8 V, the NCM contribution to capacitance and surface area further increases to values of 0.35 $F/g_{electrode}$ and 1.85 $m^2/g_{electrode}$, respectively, corresponding to an increase by a factor of ∼5.0x and ∼8.4x, respectively, as compared to the pristine state. The at first sight unexpected difference between these two factors in this case could be caused by the different domain sizes measured by the two methods: very small micropores and very thin cracks within the (primary and/or secondary) NCM particles[48–50] induced by the release of lattice oxygen will increase the surface roughness on an atomic scale and will contribute to the Kr-BET surface area (diameter of a krypton atom: ∼0.2 nm) but might be too small to be detected by the capacitance measurement (diameter of a solvated lithium ion: ∼1.0 nm), as already discussed in part I of this study.[21] The specific surface area of the PC-85 electrode of 1.85 $m^2/g_{electrode}$ after cycling to 4.8 V corresponds to 2.05 $m^2/g_{NCM}$, which may be compared to the Kr-BET area of an NCM811 material with the same initial BET area and a similar particle morphology, which after a few cycles to 4.5 V vs. $Li^+$/Li also substantially increased to ∼1.8 $m^2/g_{NCM}$.[16] In addition, the

overestimation of the CAM surface area obtained by Kr-BET could stem from additional surface area contributed by a porous organic surface layer on the positive electrode (often referred to as *cathode-electrolyte interphase* or *CEI*);[51] the formation of such a phase would result from the electrochemical oxidation of the solvents in the electrolyte at high potentials[8] or via chemical electrolyte oxidation by singlet oxygen released at high SOCs[17,18] and, therefore, lead to an overestimation of the Kr-BET surface area of the electrode cycled to 4.8 V.

Summarizing the findings in this section, one can state that electrochemical cycling beyond the limit of oxygen release at high SOCs does increase the NCM specific surface area to greater extent (~8.4-fold at 4.8 V for PC-85) as compared to cycling to lower SOCs (~1.8-fold at 4.1 V for PC-85).

***Simultaneity of lattice oxygen release, capacity fading, and surface area increase.—***Since it was found by Jung et al. that the onset of the release of lattice oxygen occurs at ~80 %SOC for NCMs with a wide range of nickel content, i.e., that it is largely a function of the degree of delithiation, the analysis of the cycling data as a function of the degree of delithiation $x$ (as in $Li_{1-x}MO_2$, with M = Ni, Co, Mn) or state of charge (in units of %SOC) will provide further insights when examining the correlation between oxygen release, capacity fading, and capacitance increase. By the analysis of the potential curves from NCM half-cells charged to 5.0 V vs. $Li^+/Li$ at the essentially same mass specific current density as those used in Fig. 4 (see Fig. A·2 in the appendix), each one of the applied upper cutoff potentials (i.e., 3.9 V, 4.0 V, …, 5.0 V vs. $Li^+/Li$) can be assigned to its respective degree of delithiation $x$, whereby $x = 1$ corresponds to a specific capacity of ~275 $mAh/g_{NCM}$ or to an SOC of 100 %SOC. Thus, Fig. 6a shows the oxygen evolution as a function of the SOC either in units of $mAh/g_{NCM}$ (upper x-axis) or in percent (lower x-axis) with the onset of the lattice oxygen release at ~80 %SOC being marked by the dashed vertical line, whereby the data are taken from Fig. 3a. Figure 6b is based on the specific discharge capacity data shown in Fig. 4a, plotting the value for the third cycle at each upper cutoff potential setpoint as a function of its degree of delithiation $x$ or its SOC that is expected based on the first charge curves shown in Fig. A·2 in the Appendix (note that ideally the difference between the actual discharge capacity and the thus obtained $x$ or SOC value corresponds to the irreversible capacity of the first cycle of the NCM active material). The data of the specific NCM capacitance shown in Fig. 4c were re-plotted analogously in Fig. 6c as a function of SOC.

Below ~85 %SOC, the specific discharge capacity of the three NCMs increases linearly, as depicted in Fig. 6b, corresponding to a linear relation between the charge capacity (x-axis, converted from the upper cutoff potential from the first charge curve) and the discharge capacity (y-axis, measured for each set of three cycles shown in Fig. 4a), indicating a stable cycling performance and, therefore, sufficient integrity of the NCMs in this SOC range. When the SOC exceeds the onset of lattice oxygen release by more than ~5 %SOC, the discharge capacity decreases as compared to the linear behavior observed for upper cutoff potentials that do not lead to delithiation degrees that are higher than ~80 %SOC. As we used pre-lithiated LTO as counter electrode, providing a substantial lithium reservoir, the specific discharge capacity decrease at >80 %SOC cannot be caused by a loss of cyclable lithium in the cell (also confirmed by the potential profile of the LTO counter electrode vs. the reference electrode, which stays on its plateau at 1.55 V vs. $Li^+/Li$ (data not shown)), but instead must be assigned to an NCM material loss and/or a significant overpotential growth of the NCM working electrode. This capacity loss can be explained by the surface reconstruction of the NCM particles into a resistive rock-salt-type surface layer upon the release of lattice oxygen, which according to previous studies with NCM811[14,16] leads to i) a cathode active material loss, as the layered structure is converted into an inactive rock-salt-type phase, and ii) an increase in the cathode impedance, caused by an increased charge-transfer resistance on the surface of the primary crystallites, a reduced electronic conductivity through the NCM secondary particles, or a combination of both. Due to these effects, the maximum discharge capacity of the two polycrystalline materials is limited to a value of ~223 $mAh/g_{NCM}$, which is reached at ~4.8 V vs. $Li^+/Li$ for PC-60 (corresponding to ~93 %SOC, red curve in Fig. 6b) and at ~4.6 V vs. $Li^+/Li$ for PC-85 (corresponding to ~89 %SOC, blue curve). Even though the single-crystalline SC-85 has essentially the same composition as the polycrystalline PC-85, it reaches its maximum discharge capacity already at ~4.4 V vs. $Li^+/Li$ (corresponding to ~85 %SOC, green curve) at a ~15 $mAh/g_{NCM}$ lower specific discharge capacity

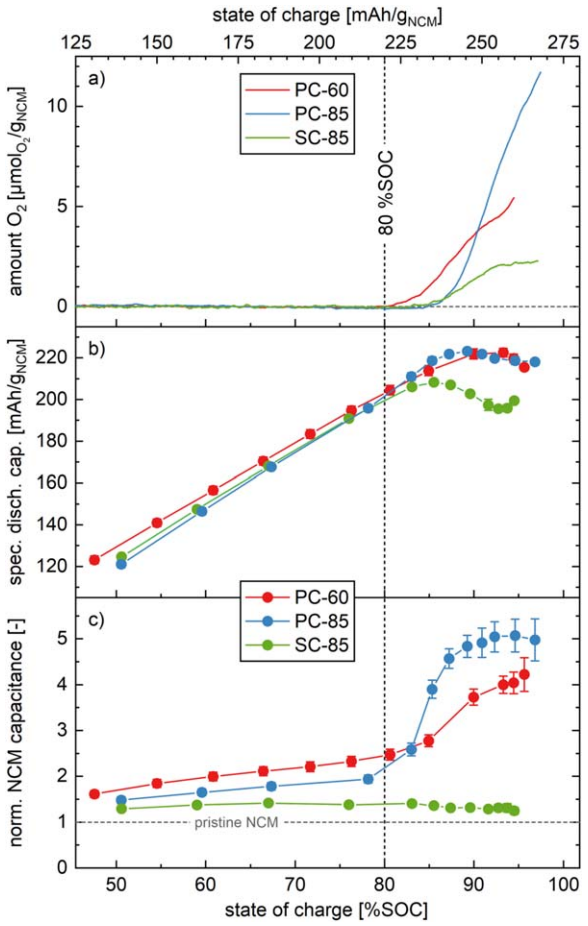


**Figure 6.** Comparison of the electrochemical characteristics of the three NCMs plotted as a function of SOC (at the top in $mAh/g_{NCM}$, at the bottom in units of %SOC corresponding to the degree of delithiation $x$ in $Li_{1-x}MO_2$), where the value for ~80 %SOC is marked by the vertical dashed line. The relation between upper cutoff potential of the NCM electrode for the cycling data in Fig. 4 and the SOC was extracted from the potential curves of the first charge of the NCM half-cells charged to 5.0 V vs. $Li^+/Li$ at the essentially identical rate of 18.4 $mA/g_{NCM}$ (see Fig. A·2 in the Appendix). **a)** Amount of oxygen normalized to the NCM mass that is detected during a CC charge at 18.4 $mA/g_{NCM}$ to 5.0 V vs. $Li^+/Li$ (same data as in Fig. 3b). **b)** Specific discharge capacity of the cells cycled to an increasing upper cutoff potential of the NCM electrode. The here plotted data correspond to those obtained in the third cycle of each upper cutoff potential shown in Fig. 4a. **c)** Capacitance contributed by the NCM particles in the NCM electrodes, normalized by their capacitance of the pristine NCM. The here plotted data correspond to those obtained in the third cycle of each upper cutoff cathode potential shown in Fig. 4c, whereby the NCM capacitance contribution to the total electrode capacitance was obtained by subtracting the capacitance contribution of the VGCF electrode (the thus obtained NCM capacitances are normalized by the NCM mass and shown in Fig. A·1 in the Appendix). The error bars are determined by the laws of error propagation (see supporting information of part I of this study),[21] using the average capacitances and their minimum/maximum values given by Fig. 4c.

(~208 mAh/$g_{NCM}$), which is attributed to the difference in morphology and will be discussed below in the context of Fig. 7. After the capacity fading of SC-85 starting at ~80 %SOC, a small increase of the discharge capacity is observed above 94 %SOC (or 4.8 V): here, we assume that the oxygen-depleted surface layer is limited in its thickness (and, therefore, in its resistance) due to the sluggish solid-state diffusion of oxygen in the NCM lattice, even though the upper cutoff potential is increased. If the growth of the surface resistance stagnates while the driving force to (de)intercalate lithium ions is increased, the increasing upper cutoff potential results in the extraction of more lithium ions and in the increase the discharge capacity for the cycles to 4.9 V and 5.0 V.

The NCM capacitance depicted in Fig. 6c is obtained by the subtraction of the contribution of the inert components VGCF and PVDF from the electrode capacitance (for details, see Figs. 4c and 5 in the previous sections and Fig. A·1 in the appendix), normalized by its pristine value, and depicted as a function of SOC. In this representation, the NCM capacitance of the two polycrystalline materials increases suddenly when charged to >80 %SOC, simultaneously with the release of lattice oxygen and the levelling-off/drop of the discharge capacity curve in Fig. 6b. Compared to their pristine state, the capacitance of the PC-60 and PC-85 active materials determined at the end of the experiment after cycling to 5.0 V vs. $Li^+$/Li changed by ~4.2x and ~5.0x, respectively, while that of the SC-85 active material changed by ~1.2x only, illustrating the morphological stability of single-crystalline NCMs even at high degrees of delithiation.

For the possible formation of an organic layer on the NCM surface at high potential, as discussed in the previous section on the validation by Kr-BET, no effect is visible of the capacitance measurements of the NCMs: SC-85 shows a stable capacitance (after the formation of a few cycles is completed, see green data in Figs. 4 and 6) up to an upper cutoff potential of 5.0 V vs. $Li^+$/Li, where a significant amount of electrolyte oxidation occurs for the here used organic electrolyte.[8] We believe that it would be a curious coincidence if the effect of hypothetical particle cracking of the single-crystalline NCM (leading to an increase in the capacitance) and the effect of an organic surface layer on the capacitance would cancel each other out perfectly for each measurement point at each upper cutoff potential. Therefore, we believe that there is no impact of a possible CEI formation on the surface-area-normalized capacitance of the NCMs in this experiment.

Under the reasonable assumption that the surface-area-normalized capacitance (~28 $\mu F_{NCM}/cm^2_{NCM}$) determined for the pristine materials (see Table I) remains constant, the specific surface area calculated from the capacitance ($S_{EIS}$) can be estimated for the NCM materials at any point of the procedure. At 5.0 V (cycle #36 in Fig. 4c or in Fig. A·1), the specific surface area $S_{EIS}^{\#36}$ is estimated to be ~1.3 $m^2/g_{NCM}$ for both polycrystalline materials (PC-60 and PC-85), whereas it is only half as large for the single-crystalline material (SC-85) that equates to 0.63 $m^2/g_{NCM}$. If one assumes spherical NCM particles and takes into account the NCM crystallographic density of $\rho_{NCM} \approx 4.63$ g/cm$^3$, the specific surface areas obtained after cycling to 5.0 V vs. $Li^+$/Li ($S_{EIS}^{\#36}$) correspond to a particle diameter of $d_p^{\#36} \approx 1.0$ µm for PC-60 and PC-85, and to 2.0 µm for SC-85, when calculated from the specific surface area $S$ by Eq. 2:

$$d = \frac{6}{S \cdot \rho_{NCM}} \quad [2]$$

The fact that the estimated diameter values for the cycled polycrystalline NCMs are still much larger than the primary crystallite size (~0.1–0.5 µm, see Fig. 2) suggests that not all primary particles within the secondary agglomerates have been exposed to the electrolyte after the cycling procedure to 5.0 V vs. $Li^+$/Li. However, here one has to consider that the capacitance measurements are taken in the fully lithiated state of the NCM particles, where initially formed cracks between the primary particles might be sealed again; such a phenomenon was observed for polycrystalline NCM811, which after a few cycles to 4.5 V vs. $Li^+$/Li had a Kr-BET area of ~1.8 $m^2$/g in the fully lithiated state and ~3.2 $m^2$/g in the charged state.[16]

To summarize the findings in this section, we were able to show that capacity loss and lattice oxygen release occur simultaneously above ~80 %SOC for the three different NCM materials, independent of their composition and morphology. Furthermore, the lattice oxygen release also induces a sudden increase in the specific surface area of polycrystalline NCMs, whereas the morphology of the single-crystalline materials seems to be maintained, as inferred from in situ capacitance measurements.

***Capacity loss in dependence of the NCM particle morphology.—***When cycled to high state of charge, the observed capacity of SC-85 (207 mAh/$g_{NCM}$ at 4.5 V in cycle #21, see Fig. 4a or Fig. 6b) is significantly diminished when compared to PC-85 (222 mAh/$g_{NCM}$), and since these materials have the identical composition, the observed difference must stem from the difference in particle morphology. To illuminate this effect further, the potential curves of charge and discharge as well as the respective specific differential capacity curves (often referred to as d$q$/d$V$ plot) are presented in Fig. 7**,** both extracted from the electrochemical cycling data shown in Figs. 4 and 6.

During cycle #9 with an upper cutoff potential of the NCM electrode of 4.1 V vs. $Li^+$/Li, which corresponds to ~69 %SOC and is thus still below the onset potential of the lattice oxygen release for both PC-85 and SC-85 (detected at 4.23 V or ~80 %SOC), the potential curves (see Fig. 7a) and the specific differential capacities (see Fig. 7b) coincide, yielding the same discharge capacity of 186 mAh/$g_{NCM}$.

In contrast, after three cycles to 4.5 V vs. $Li^+$/Li (cycle #21, corresponding to ~89 %SOC), the features of the potential curve of the single-crystalline SC-85 material (green), shown in Fig. 7c, are not only shifted to lower capacities by ~15 mAh/$g_{NCM}$ as compared to PC-85 (blue), e.g., when comparing the position of the plateau at ~4.2 V, but the entire curve also shows a ~40 mV higher overpotential as compared to PC-85, which can also be seen by the shift of all d$q$/d$V$ features of SC-85 during both charge and discharge (see Fig. 7d). Furthermore, the capacity which is contributed during the H2-H3 phase transition (marked by the plateau in Fig. 7c or the peak in Fig. 7d at ~4.2 V) is significantly smaller for the single-crystalline SC-85 material. When increasing the upper cutoff potential of the NCM electrode to 4.8 V vs. $Li^+$/Li (cycle #30, ~94 %SOC), these differences between the poly- and the single-crystalline NCM increase: the potential curve of SC-85 is shifted by ~20 mAh/$g_{NCM}$ to lower capacities and it has a ~100 mV higher overpotential for both charge and discharge as compared to the PC-85 material (see Fig. 7e), which becomes clear when comparing the shift of the d$q$/d$V$ features (see Fig. 7f); at the same time, the H2-H3 feature disappears almost completely for the charge of the SC-85 material. Overall, a loss of the discharge capacity of 24 mAh/$g_{NCM}$ is observed for SC-85 (196 mAh/$g_{NCM}$) as compared to PC-85 (220 mAh/$g_{NCM}$).

When cycled to 4.8 V vs. $Li^+$/Li in cycle #30, a potential difference of ~210 mV is observed between the charge and discharge curve at 137.5 mAh/$g_{NCM}$ (corresponding to ~50 % SOC) for SC-85 in Fig. 7e, whereas only ~60 mV or ~30 % of the value of SC-85 are detected for PC-85. If we assume that the overpotential for charge and discharge are identical for the SC-85 material (i.e., ~105 mV), this corresponds to a mass specific electrode resistance of ~4.9 Ω·$g_{NCM}$ when considering the applied current of 21.4 mA/$g_{NCM}$; for the given NCM loading of 8.7 $mg_{NCM}/cm^2_{electrode}$, this translates to a very large areal resistance of ~0.56 kΩ·$cm^2_{electrode}$. At the current state, we assign this resistance to the NCM charge-transfer reaction, which is significantly hindered by the formation of an oxygen-depleted surface layer. A similar resistance increase of an oxygen-depleted surface layer was previously shown by Pritzl et al., inducing the oxygen

release and the subsequent resistance increase through washing and heating.[52] In principal, the difference in overpotential of PC-85 and SC-85 and the subsequent capacity loss could stem from the difference in morphology, as, according to the above analysis of the capacitance data, the polycrystalline PC-85 material provides a ∼2-fold higher specific surface area as compared to the single-crystalline SC-85 when charged to high SOCs (∼1.3 $m^2/g_{NCM}$ vs. ∼0.63 $m^2/g_{NCM}$, as discussed above): at a ∼2-fold higher specific surface area and at the same applied specific current (in units of $mA/g_{NCM}$), the surface-area-normalized current density (in units of $mA/m^2_{NCM}$) for the polycrystalline PC-85 material would be ∼50 % lower; this appears as a ∼2-fold lower charge-transfer resistance and thus a ∼2-fold lower overpotential for PC-85, assuming that the surface and bulk properties of the two NCM851005 materials with regards to the (de)lithiation kinetics are the same. Here, however, it must be considered that the exposed NCM surface area for a polycrystalline NCM can be up to ∼2-fold larger in its delithiated state compared to its lithiated state in which the capacitance measurements were made, as demonstrated for a polycrystalline NCM811 by means of Kr-BET.[16] If this were to apply also to the here used PC-85 material, which has the same particle morphology as the NCM811 material of the latter study, it would predict an up to ∼4-fold higher surface area. As the total charge-transfer resistance of an active material scales inversely with its total active material surface area, the resistance and, therefore, the overpotential is increased ∼4-fold at the same specific current for the single-crystalline SC-85 as compared to the polycrystalline PC-85 material. Within this uncertainty, the observed differences in overpotential between the PC-85 and the SC-85 material could be explained entirely by the differences in exposed surface area.

Furthermore, the suppressed H2-H3 phase transition of SC-85, seen in Fig. 7f at ∼4.2–4.3 V, might be caused by a mechanism mainly occurring at high SOC: Xu et al.[53] showed that the lattice mismatch of the layered bulk structure and the oxygen-depleted (rock-salt-type) surface layer hinders the development of the H3 phase in the bulk of the primary particles and, therefore, the extraction of lithium above ∼75 %SOC. This lattice mismatch, which occurs only at high SOCs, induces an additional kinetic hindrance of the H2-H3 phase transition in the NCM during charge. Due to the ∼4-fold lower surface area of the single-crystalline material as well as its respectively larger primary crystallite size, this effect might emerge to a higher extent for SC-85, limiting the capacity obtained from the H2-H3 phase transition at ∼4.2–4.3 V. In discharge, however, the H2-H3 phase transition of SC-85 delivers a similar (differential) capacity as the one of PC-85, which can only be explained by the higher charge capacity of SC-85 above 4.3 V (30 $mAh/g_{NCM}$ for SC-85 between 4.3 V and the end of the CV hold at 4.8 V as compared to 19 $mAh/g_{NCM}$ for PC-85, see Fig. 7e), as also the differential charge capacity of SC-85 above 4.3 V is permanently increased as compared to the one PC-85 (see Fig. 7f). This observation shows that the H2-H3 phase transformation of SC-85 does take place when cycled to 4.8 V vs. $Li^+$/Li but is kinetically hindered during charge (i.e., during delithiation), which is why the H2-H3 feature in the d$q$/d$V$ is diminished while its capacity is delivered at higher potentials.

In the end, the combination of the ∼4-fold higher overpotential caused by the difference in surface area as well as the suppressed H2-H3 transition enhance the loss of discharge capacity for the single-crystalline SC-85 material when cycled to high SOC. However, one should note that in actual commercial battery cells with single-crystalline NCMs such high cathode potential cutoffs of 4.8 V vs. $Li^+$/Li would not be used for nickel-rich NCMs, so that the here observed very large increase in overpotentials and the associated large capacity losses would not be observed. The effect of the morphology on the long-term cycling performance of the here used materials in full-cells will be discussed in an independent publication.

Based on the results of this section, we conclude that stable cycling of conventional NCMs is limited to degrees of delithiation

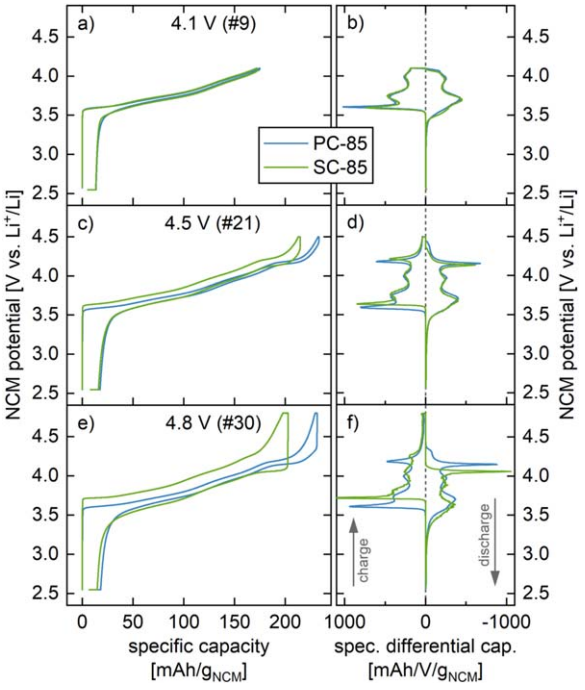


**Figure 7.** Comparison of the (dis)charge curves of PC-85 (blue) and SC-85 (green). The potential curves, showing the NCM potential vs. $Li^+$/Li as a function of the specific capacity, were extracted from the electrochemical cycling data shown in Fig. 4, here depicted in separate panels for the third cycle to **a)** 4.1 V (#9), **c)** 4.5 V (#21), and **e)** 4.8 V (#30). The respective specific differential capacity (often referred to as d$q$/d$V$ plot) as a function of the NCM potential, derived from the potential curves, is presented in separate panels for the same cycles to **b)** 4.1 V (#9), **d)** 4.5 V (#21), and **f)** 4.8 V (#30). Here, the charge is shown on the positive x-axis (left half of the right panels) and the discharge on the negative one (right half); also, the x- and y-axis are switched as compared to the conventional representation for an easier comparison with the potential curves. Distinct redox features or phase transitions appear as peaks, corresponding to plateau-like regions in the potential profiles. The NCM potential was calculated from the full-cell potential, based on the potential of 1.55 V vs. $Li^+$/Li of the pre-lithiated, capacitively oversized LTO which was used as counter electrode.

<85 %SOC, independent of their composition or morphology. However, single-crystalline NCM particles having a concentration gradient of the transition metals (as previously reported for poly-crystalline NCMs)[54,55] with a nickel-rich core (e.g., a nickel content of >85 %) and a surface layer region with a lower nickel content (e.g., 60 % nickel) could circumvent this limit: if such a material could be synthesized, and if it cycled without cracking of the primary crystallites (not exposing the nickel-rich core to the electrolyte), one could delithiate this material to an upper cutoff potential of 4.50 V (stability limit of NCM622 at ∼80 %SOC or 220 $mAh/g_{NCM622}$, see Figs. 3 and A·2); in contrast, the nickel-rich core would have delivered 240 $mAh/g_{NCM851005}$ (for NCM851005, 87 %SOC of its theoretical capacity, see Fig. A·2) or 257 $mAh/g_{LNO}$ (for LNO, 93 %SOC)[6] at this potential, which could increase the provided cathode energy density in future lithium-ion batteries by ∼10 % or even up to ∼17 %, respectively.

***Mechanisms causing the surface area increase.—***In the following, possible reasons for the surface area increase observed for the polycrystalline NCMs occurring simultaneously with the oxygen release at high SOC are discussed:

- The capacitance increase of the polycrystalline NCMs, associated with an increase in specific surface area (proven by Kr-BET measurements), could be caused by the cracking of the primary crystallites upon the release of lattice oxygen. It has been reported that the delamination/exfoliation of the layered NCM structure might

**Table I. Overview of the experimental results. Pristine NCM and VGCF-only powders/electrodes: specific surface areas of the material powders measured by Kr-BET ($S_{BET}$) and respective particle diameters $d_p$ (calculated from $S_{BET}$), specific NCM and VGCF electrode capacitance (measured by EIS, from Fig. 4c), specific NCM capacitance contribution to the electrodes (from Fig. A·1 in the Appendix), and surface-area-normalized capacitance of NCMs or VGCF (normalized by $S_{BET}$). Electrodes cycled to 5.0 V vs. $Li^+$/Li (cycle #36): specific electrode capacitance (measured by EIS, from Fig. 4c), specific NCM capacitance (from Fig. A·1 in the Appendix), specific surface area ($S_{EIS}^{\#36}$) calculated from the specific NCM capacitance and the surface-area-normalized capacitance of the pristine electrodes, NCM particle diameter ($d_p^{\#36}$) calculated from $S_{EIS}^{\#36}$, and specific surface area change (comparing $S_{BET}$ and $S_{EIS}^{\#36}$). Also shown are the specific amounts of oxygen ($O_2$) and carbon dioxide ($CO_2$) as well as their sum ($O_2$+$CO_2$) detected by OEMS during a charge to 5.0 V and normalized by the NCM mass (from Fig. 3), from which the fraction of NCM converted from a layered structure to a rock-salt-type reconstructed surface phase ($y$) and the respective layer thickness ($d_l$) were calculated.**

| | Electrode material | Units | PC-60 | PC-85 | SC-85 | Units | VGCF only |
|---|---|---|---|---|---|---|---|
| Pristine | Specific surface area $S_{BET}$ | $m^2_{NCM}/g_{NCM}$ | 0.32 | 0.27 | 0.51 | $m^2_{VGCF}/g_{VGCF}$ | 12.4 |
| | Particle diameter $d_p$ (from $S_{BET}$) | µm | 4.0 | 4.8 | 2.6 | – | – |
| | Specific electrode capacitance | $F/g_{electrode}$ | 0.12 | 0.11 | 0.17 | $F/g_{electrode}$ | 0.43 |
| | Specific material capacitance | $F_{NCM}/g_{NCM}$ | 0.09 | 0.08 | 0.14 | $F_{VGCF}/g_{VGCF}$ | 0.54 |
| | Surface-area-norm. capacitance | $\mu F_{NCM}/cm^2_{NCM}$ | 27 | 29 | 28 | $\mu F_{VGCF}/cm^2_{VGCF}$ | 4.4 |
| At 5.0 V vs. $Li^+$/Li (cycle #36) | Specific electrode capacitance | $F/g_{electrode}$ | 0.37 | 0.39 | 0.20 | | |
| | Specific NCM capacitance | $F_{NCM}/g_{NCM}$ | 0.36 | 0.38 | 0.17 | | |
| | Specific surface area $S_{EIS}^{\#36}$ | $m^2_{NCM}/g_{NCM}$ | 1.34 | 1.33 | 0.63 | – | |
| | Particle diameter $d_p^{\#36}$ (from $S_{EIS}^{\#36}$) | µm | 1.0 | 1.0 | 2.0 | | |
| | Specific surface area change | – | 4.2x | 5.0x | 1.2x | | |
| | Detected specific $O_2$ amount | $\mu mol_{O_2}/g_{NCM}$ | 5.4 | 11.7 | 2.5 | | |
| | Detected specific $CO_2$ amount | $\mu mol_{CO_2}/g_{NCM}$ | 64.1 | 195.2 | 114.0 | | |
| | Detected specific $O_2$+$CO_2$ amount | $\mu mol_{O_2+CO_2}/g_{NCM}$ | 69.5 | 206.9 | 116.6 | – | |
| | Oxygen-depleted fraction $y$ | – | 0.013 | 0.040 | 0.023 | | |
| | Rock-salt-type layer thickness $d_l$ | nm | 1.0 | 3.0 | 3.6 | | |

be favored by the formation of a rock-salt-type phase which initiates the delamination of the layers either from the surface, from the bulk, or from nanopores of the primary crystallites.[49,50,56] Since the capacitance of the single-crystalline SC-85 material only changes by a factor of less than ~1.4x, which could be explained by cracking of the interfaces between the large single-crystals (see Fig. 2c), a significant contribution from the cracking of the primary crystallites to the capacitance increase of the polycrystalline NCMs (with numerous primary crystallites forming secondary agglomerates) upon lattice oxygen release seems unlikely. However, it must be noted that the cells are cycled in this experiment for 36 cycles only, all at rather slow rates and only at 25 °C. As an accelerated degradation of the cell performance is typically observed during long-term cycling at higher rates and elevated temperatures, the potential cracking of the primary crystallites under harsher conditions can occur and has indeed been observed.[57,58]

- Under the here examined conditions, an irreversible opening of the void spaces between the primary crystallites seems to be more likely than the cracking of the primary particles. Here, it has to be noted that the capacitance is measured in the discharged state only, therefore, tracking only irreversibly opened pores; it was observed previously that small cracks are able to re-seal upon lithiation.[16,59] Upon the release of lattice oxygen, the near-surface region of the NCM particles reconstruct into an oxygen-depleted surface layer around each of the primary crystallites that are exposed to the electrolyte.[14] This phase, often reported to be a rock-salt-type phase,[60] has a primitive cell volume which is significantly reduced as compared to the layered structure. For LNO, being similar to the nickel-rich NCMs, the primitive cell volume decreases by 54 % when the structure is converted from $LiNiO_2$ ($V = 39.3$ Å$^3$)[6,7,61] to NiO ($V = 18.2$ Å$^3$),[62,63] a much larger volume change compared to that which occurs upon (de)lithiation (only ~9 %).[7,61] Through this reduction of the material volume upon surface reconstruction, mechanical stresses are likely induced that lead to crack formation between the primary particles, which in turn leads to the penetration of the secondary agglomerates by the electrolyte and to the here observed increase of the capacitance and the Kr-BET.
- Finally, the released lattice oxygen partially reacts with the organic electrolyte components, forming protic species by the chemical oxidation of, e.g., ethylene carbonate (EC).[3,17,18] Lithium compounds like lithium carbonate and lithium oxide that may have remained on the surface of the primary crystallites from the synthesis, would then be chemically decomposed by the protons in the electrolyte, exposing the primary crystallites and increasing the surface area of polycrystalline NCMs.[34]

From the presented data, we expect a combination of the latter two mechanisms to cause the surface area increase at high state of charge. The apparent surface area increase observed for polycrystalline NCMs might give rise to capacity fading in full-cells, caused by loss of electronic contact in the secondary agglomerate[14,64,65] as well as by enhanced side reactions, including gas evolution,[3] electrolyte oxidation,[8,18] proton generation,[34] transition metal dissolution with subsequent deposition on the anode leading to additional SEI growth and loss of cyclable lithium,[19,20,66] as well as loss of active material.[14] For commercial cells, single-crystalline materials with an appropriate particle size are expected to provide an improved long-term performance, as they maintain their specific surface area upon cycling.

***Estimation of the thickness of the oxygen-depleted surface layer.***—Even though the pristine specific surface area of the SC-85 material (0.51 $m^2/g_{NCM}$) is larger as compared to PC-85 (0.27 $m^2/g_{NCM}$), smaller amounts (~50 %) of molecular oxygen ($O_2$) and carbon dioxide ($CO_2$) are detected for the former (see Fig. 3). This can only be explained through a significant surface area increase of PC, if one assumes a similar film thickness of the oxygen-depleted surface layer, what seems reasonable based on the identical NCM composition. As the surface area increase of polycrystalline NCMs at high state of charge (see Fig. 6) has not been considered for the estimation of the

oxygen-depleted surface layer thickness, previous studies may have significantly overestimated its thickness. With the precise in situ quantification of the specific surface area of the NCM particles, a more reliable value for the oxygen-depleted surface layer thickness is now provided based on the detected amounts of $O_2$ and $CO_2$.

In contrast to the $O_2$ evolution, the generation of $CO_2$ is not only caused by the release of (singlet) oxygen and its chemical reaction with the electrolyte, but also partially by the decomposition of $Li_2CO_3$ and the electrochemical oxidation of electrolyte components at 5.0 V vs. $Li^+/Li$, prohibiting to discriminate the $CO_2$ amounts caused by the release of lattice oxygen from the other mechanisms. By taking the sum of the amounts of $O_2$ and $CO_2$ (in units of $\mu mol_{O_2+CO_2}/g_{NCM}$) released at 5.0 V to represent the total amount of released lattice oxygen, an upper limit of the released lattice oxygen and, hence, of the thickness of the oxygen-depleted surface layer can be determined. As shown in Fig. 3 and summarized in Table I, the total amounts of the evolved gases are 69.5 $\mu mol_{O_2+CO_2}/g_{NCM}$ for PC-60, 206.9 $\mu mol_{O_2+CO_2}/g_{NCM}$ for PC-85, and 116.6 $\mu mol_{O_2+CO_2}/g_{NCM}$ for SC-85. If the surface reconstruction of the layered structure to a rock-salt-type phase occurs according to the following reaction,

$$Li_{1-x}MO_2 \rightarrow (1-y)\, Li_{\frac{1-x}{1-y}}MO_2 + y\, MO + \frac{y}{2} O_2 \qquad [3]$$

0.5 $mol_{O_2}$ are released per 1 $mol_{NCM}$ that is reconstructed into a rock-salt-type phase. From Eq. 3, together with the above assumption that the actual amount of released lattice oxygen is represented by the sum of detected $O_2$ and $CO_2$ (0.5 $mol_{O_2+CO_2}$), the fraction $y$ of the NCM material that was converted to a rock-salt-type surface layer can be calculated from the ratio of the detected gas amounts (in $\mu mol_{O_2+CO_2}/g_{NCM}$) and the gas amounts calculated for a complete conversion to a rock-salt-type phase (0.5 $mol_{O_2+CO_2}/mol_{NCM}$), taking into account the NCM molar mass ($M_{NCM}$ = 96.9 $g_{NCM}/mol_{NCM}$ for PC-60 and 97.5 $g_{NCM}/mol_{NCM}$ for PC-85 and SC-85).

For PC-60, the observed 69.5 $\mu mol_{O_2+CO_2}/g_{NCM}$ correspond to a converted fraction $y = 0.013$, whereas values of 0.040 and 0.022 are obtained for PC-85 and SC-85, respectively. As previously done by Jung et al. using a spherical approximation,[3] the thickness of the oxygen-depleted surface layer $d_l$ can be estimated by Eq. 4, taking the ratio of the volume of the entire particle ($V_p$) and the one of the oxygen-depleted layer ($V_l$):

$$y = \frac{1}{0.46}\frac{V_l}{V_p} = \frac{1}{0.46}\frac{((d_p)^3 - (d_p - d_l)^3)}{d_p^3} \qquad [4]$$

Here, the estimated particle diameter $d_p^{\#36}$ of the three NCMs at 5.0 V (see Table I) is taken into account as well as the required correction factor of 0.46 which considers the volume difference of $Li_{1-x}MO_2$ and MO, as, e.g., for LNO (as the lattice parameters for rock-salt-type phase of the various NCMs are not available), the primitive cell volume of the rock-salt-type phase is only 46 % as compared to the one of the layered phase (see discussion above). For PC-60, a rock-salt-type layer thickness of the exposed primary crystallites of 1.0 nm is obtained when charged once to 5.0 V, whereas for PC-85 and SC-85, both having a higher nickel content, similar film thicknesses of 3.0 nm and 3.6 nm are estimated, respectively. Hereby, one should note that the film thicknesses of the polycrystalline NCMs would be overestimated by a factor of 4.2x or 5.0x, respectively, if the surface area increase at high SOC would not be taken into account. We believe that the increased film thickness of PC-85 and SC-85 as compared to PC-60 is caused by the increased nickel content, destabilizing the layered structure due to the high reactivity of $Ni^{4+}$, as this has been assigned multiple times to, e.g., a decreased thermal stability as well as an increased reactivity towards moisture.[4,61,67–69] Further, a higher solid-state diffusion of oxygen in the structure of layered oxides with a higher nickel content could lead to more lattice oxygen being released upon delithiation to high SOC, what has not yet been reported to the best of our knowledge.

In summary, we were able to calculate the thicknesses of the oxygen-depleted surface layer, which were larger for NCMs with a higher nickel content and similar for NCMs with the same NCM composition, independent of the particle morphology when the gas amounts detected by OEMS were normalized to the surface area obtained by the capacitance measurements upon cycling.

## Conclusions

The correlation of oxygen release, capacity fading, and particle cracking was investigated as a function of state of charge for three nickel-rich NCMs, differing either in composition (i.e., in transition metal ratio) or in morphology (i.e., in primary crystallite size of the poly- and single-crystalline NCMs). First, the onset of the release of lattice oxygen was observed at ~80 %SOC by OEMS, independent of the nickel content. In electrochemical cycling experiments, during which the NCM electrode capacitance was tracked by EIS while the upper cutoff potential was increased every third cycle stepwise from 3.9 V to 5.0 V, a fading of the discharge capacity occurred at high degree of delithiation when the onset of oxygen release was exceeded by ~10 %SOC. Simultaneously, the specific surface area of the polycrystalline NCMs increased suddenly at high SOC to more than 400 % of the pristine one, which was determined by the capacitance extracted from the impedance spectra using a micro-reference electrode (μ-RE) and validated through Kr-BET measurements of cycled electrodes. In contrast, the specific surface area of the single-crystalline NCM changed by less than 40 %, even after complete delithiation, highlighting the morphological stability of single-crystalline cathode active materials.

The lower specific surface area retained by the single-crystalline material upon cycling, however, enhanced the detrimental effect of the resistive oxygen-depleted surface layer formed upon release of lattice oxygen, leading to lower discharge capacities at high SOC compared to the polycrystalline materials. Owing to the morphological integrity of the crystallites of the single-crystalline NCM, its long-term cycling performance in full-cells with commonly used upper cutoff potentials, however, is expected to be improved, as the side reactions that consume cyclable lithium are diminished due to its lower specific surface area upon cycling. From the detected amounts of evolved gases and the determined specific surface areas, the thickness of the reconstructed rock-salt-type surface layer was estimated to be ~3-4 nm for NCM851005, independent of the particle morphology, and ~1 nm for NCM622. To enable a broader accessibility of this powerful and non-destructive impedance-based method tracking the NCM particle cracking in situ, a simplified cell setup – without reference electrode and without the need for a pre-lithiated LTO electrode – will be introduced in part III of this study.

## CRediT Authorship Contribution Statement

Stefan Oswald: Methodology, Investigation, Writing—Original Draft. Daniel Pritzl: Methodology, Writing—Review & Editing. Morten Wetjen: Methodology, Writing—Review & Editing. Hubert A. Gasteiger: Conceptualization, Supervision, Writing—Review & Editing.

## Acknowledgments

Stefan Oswald and Dr. Daniel Pritzl gratefully acknowledge the BASF Battery Research Network for its financial support. Funding for Dr. Morten Wetjen was provided by the German Federal Ministry for Economic Affairs and Energy (BMWi, funding number 03ET6045D). Xiaohang Liu and BASF SE (Germany) are kindly acknowledged for providing the active materials. The authors also kindly thank Felix Riewald (BASF SE) for fruitful discussions.

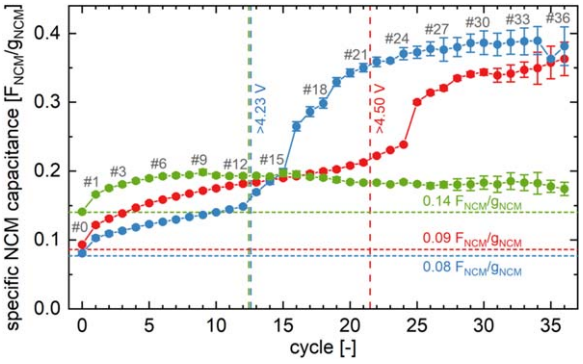


**Figure A·1.** Specific NCM capacitance of PC-60 (red), PC-85 (blue), and SC-85 (green) as working electrodes (in units of $F_{NCM}/g_{NCM}$) as a function of cycle number, calculated from the specific electrode capacitance in Fig. 4c by subtracting $1/10^{th}$ of the contribution of the VGCF electrode (0.1x of 0.43 $F/g_{electrode}$) and subsequently normalized by the NCM mass. The horizontal dashed lines indicate the pristine NCM capacitance value of each of the three NCM materials before the conditioning step (#0), whereas the vertical dashed lines mark the cycle at which ~80 %SOC (extracted from Fig. 3) are exceeded for each of the three NCMs (4.50 V for PC-60, and 4.23 V for PC-85 and SC-85), marking the onset of the release of lattice oxygen observed in Fig. 3. The error bars are determined by the laws of error propagation (see supporting information of part I of this study),[21] using the average capacitances and their minimum/maximum values given in Fig. 4c.

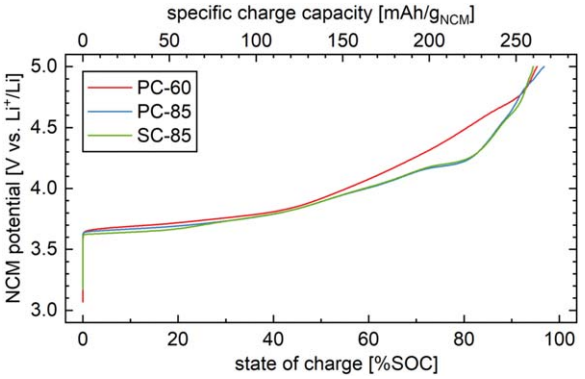


**Figure A·2.** Potential curves of the first charge of the three NCMs as a function of the specific charge capacity (in units of $mAh/g_{NCM}$ at the top) or state of charge (in %SOC at the bottom, corresponding to the degree of delithiation $x$ in $Li_{1-x}MO_2$), respectively. Cells were assembled with PC-60 (red), PC-85 (blue), or SC-85 (green) as working electrodes in T-cells with 90 µl LP57, and lithium metal as counter electrode and reference electrode (with three glass fiber separators, two placed between the working and the counter electrode as well as one toward the reference electrode). Controlled by the reference electrode potential, the NCM electrodes were charged at 25 °C to 5.0 V vs. $Li^+/Li$ at a current of 18.4 $mA/g_{NCM}$ (corresponding to a *C*-rate of *C*/15 when referenced to the theoretical capacity of ~275 $mAh/g_{NCM}$).

## Appendix

To be able to quantify the relative increase of the capacitance of the NCM materials only, the contribution of the inert electrode components VGCF and PVDF are excluded: therefor, $1/10^{th}$ of the VGCF electrode (0.1x of 0.43 $F/g_{electrode}$) was subtracted from the electrode capacitance values for each NCM material and cycle number (both shown in Fig. 4c). The obtained NCM capacitance (in units of $F_{NCM}/g_{electrode}$) was normalized by the NCM mass in the electrode (resulting in units of $F_{NCM}/g_{NCM}$), considering that the NCM content in the electrode is 90 wt% ($m_{NCM} = 0.9 \cdot m_{electrode}$), and depicted as a function of cycle number in Fig. A·1.

To allow for a better interpretation of the cycling data in Fig. 4 showing the specific discharge capacity and the specific electrode capacitance as a function of cycle number with increasing upper cutoff potentials of the NCM electrode, the latter was converted into the respective degree of delithiation ($x$ in $Li_{1-x}MO_2$, with M = Ni, Co, Mn) or state of charge (SOC), with the resulting plot being depicted in Fig. 6. For this conversion, the required relation between upper cutoff potential (i.e., 3.9 V, 4.0 V, …, 5.0 V vs. $Li^+/Li$) and the SOC was extracted from the potential curves of the first charge for each of the three NCMs under the essentially identical charging current, which are shown in Fig. A·2.

## ORCID

Stefan Oswald https://orcid.org/0000-0001-6402-7833
Daniel Pritzl https://orcid.org/0000-0002-9029-107X
Morten Wetjen https://orcid.org/0000-0002-2357-1151
Hubert A. Gasteiger https://orcid.org/0000-0001-8199-8703

## References

1. N. Nitta, F. Wu, J. T. Lee, and G. Yushin, *Mater. Today*, **18**, 252 (2015).
2. W. Li, E. M. Erickson, and A. Manthiram, *Nat. Energy*, **5**, 26 (2020).
3. R. Jung, M. Metzger, F. Maglia, C. Stinner, and H. A. Gasteiger, *J. Electrochem. Soc.*, **164**, A1361 (2017).
4. H.-J. Noh, S. Youn, C. S. Yoon, and Y.-K. Sun, *J. Power Sources*, **233**, 121 (2013).
5. H.-H. Ryu, K.-J. Park, C. S. Yoon, and Y.-K. Sun, *Chem. Mater.*, **30**, 1155 (2018).
6. H. Li, N. Zhang, J. Li, and J. R. Dahn, *J. Electrochem. Soc.*, **165**, A2985 (2018).
7. H. Li, A. Liu, N. Zhang, Y. Wang, S. Yin, H. Wu, and J. R. Dahn, *Chem. Mater.*, **31**, 7574 (2019).
8. R. Jung, M. Metzger, F. Maglia, C. Stinner, and H. A. Gasteiger, *J. Phys. Chem. Lett.*, **8**, 4820 (2017).
9. R. Jung, P. Strobl, F. Maglia, C. Stinner, and H. A. Gasteiger, *J. Electrochem. Soc.*, **165**, A2869 (2018).
10. D. Streich, C. Erk, A. Guéguen, P. Müller, F.-F Chesneau, and E. J. Berg, *J. Phys. Chem. C*, **121**, 13481 (2017).
11. D. P. Abraham, R. D. Twesten, M. Balasubramanian, I. Petrov, J. McBreen, and K. Amine, *Electrochem. Commun.*, **4**, 620 (2002).
12. S. Watanabe, M. Kinoshita, T. Hosokawa, K. Morigaki, and K. Nakura, *J. Power Sources*, **258**, 210 (2014).

13. S. K. Jung, H. Gwon, J. Hong, K. Y. Park, D. H. Seo, H. Kim, J. Hyun, W. Yang, and K. Kang, *Adv. Energy Mater.*, **4**, 1300787 (2014).
14. F. Friedrich, B. Strehle, A. T. S. Freiberg, K. Kleiner, S. J. Day, C. Erk, M. Piana, and H. A. Gasteiger, *J. Electrochem. Soc.*, **166**, A3760 (2019).
15. J. Choi and A. Manthiram, *J. Electrochem. Soc.*, **152**, 1714 (2005).
16. B. Strehle, F. Friedrich, and H. A. Gasteiger, *J. Electrochem. Soc.*, **168**, 050512 (2021).
17. J. Wandt, A. T. S. Freiberg, A. Ogrodnik, and H. A. Gasteiger, *Mater. Today*, **21**, 825 (2018).
18. A. T. S. Freiberg, M. K. Roos, J. Wandt, R. De Vivie-Riedle, and H. A. Gasteiger, *J. Phys. Chem. A*, **122**, 8828 (2018).
19. R. Jung, F. Linsenmann, R. Thomas, J. Wandt, S. Solchenbach, F. Maglia, C. Stinner, M. Tromp, and H. A. Gasteiger, *J. Electrochem. Soc.*, **166**, A378 (2019).
20. S. Solchenbach, G. Hong, A. T. S. Freiberg, R. Jung, and H. A. Gasteiger, *J. Electrochem. Soc.*, **165**, A3304 (2018).
21. S. Oswald, D. Pritzl, M. Wetjen, and H. A. Gasteiger, *J. Electrochem. Soc.*, **167**, 100511 (2020).
22. L. de Biasi, A. O. Kondrakov, H. Geßwein, T. Brezesinski, P. Hartmann, and J. Janek, *J. Phys. Chem. C*, **121**, 26163 (2017).
23. A. O. Kondrakov, A. Schmidt, J. Xu, H. Geßwein, R. Mönig, P. Hartmann, H. Sommer, T. Brezesinski, and J. Janek, *J. Phys. Chem. C*, **121**, 3286 (2017).
24. W. Li, H. Y. Asl, Q. Xie, and A. Manthiram, *J. Am. Chem. Soc.*, **141**, 5097 (2019).
25. Y. Kim, *Appl. Mater. Interfaces*, **4**, 2329 (2012).
26. G. Liu, M. Li, N. Wu, L. Cui, X. Huang, X. Liu, Y. Zhao, H. Chen, W. Yuan, and Y. Bai, *J. Electrochem. Soc.*, **165**, A3040 (2018).
27. G. Qian, Y. Zhang, L. Li, R. Zhang, J. Xu, Z. Cheng, S. Xie, H. Wang, Q. Rao, Y. He, Y. Shen, L. Chen, M. Tang, and Z.-F. Ma, *Energy Storage Mater.*, **27**, 140 (2020).
28. E. Trevisanello, R. Ruess, G. Conforto, F. H. Richter, and J. Janek, *Adv. Energy Mater.*, **2003400** (2021).
29. J. Li, A. R. Cameron, H. Li, S. Glazier, D. Xiong, M. Chatzidakis, J. Allen, G. A. Botton, and J. R. Dahn, *J. Electrochem. Soc.*, **164**, A1534 (2017).
30. J. E. Harlow, X. Ma, J. Li, E. Logan, Y. Liu, N. Zhang, L. Ma, S. L. Glazier, M. M. E. Cormier, M. Genovese, S. Buteau, A. Cameron, J. E. Stark, and J. R. Dahn, *J. Electrochem. Soc.*, **166**, A3031 (2019).
31. R. Bernhard, M. Metzger, and H. A. Gasteiger, *J. Electrochem. Soc.*, **162**, A1984 (2015).
32. N. Tsiouvaras, S. Meini, I. Buchberger, and H. A. Gasteiger, *J. Electrochem. Soc.*, **160**, A471 (2013).
33. S. Solchenbach, D. Pritzl, E. J. Y. Kong, J. Landesfeind, and H. A. Gasteiger, *J. Electrochem. Soc.*, **163**, A2265 (2016).
34. A. T. S. Freiberg, J. Sicklinger, S. Solchenbach, and H. A. Gasteiger, *Electrochim. Acta*, **346**, 136271 (2020).
35. U. Heider, R. Oesten, and M. Jungnitz, *J. Power Sources*, **81–82**, 119 (1999).
36. J. Landesfeind, D. Pritzl, and H. A. Gasteiger, *J. Electrochem. Soc.*, **164**, A1773 (2017).
37. M. Gaberscek, J. Moskon, B. Erjavec, R. Dominko, and J. Jamnik, *Electrochem. Solid-State Lett.*, **11**, A170 (2008).
38. D. Pritzl, A. E. Bumberger, M. Wetjen, J. Landesfeind, S. Solchenbach, and H. A. Gasteiger, *J. Electrochem. Soc.*, **166**, A582 (2019).
39. O. Barbieri, M. Hahn, A. Herzog, and R. Kötz, *Carbon*, **43**, 1303 (2005).
40. H. Ji, X. Zhao, Z. Qiao, J. Jung, Y. Zhu, Y. Lu, L. L. Zhang, A. H. MacDonald, and R. S. Ruoff, *Nat. Commun.*, **5**, 3317 (2014).
41. J. Chmiola, G. Yushin, Y. Gogotsi, C. Portet, P. Simon, and P. L. Taberna, *Science*, **313**, 1760 (2006).
42. L. Ramaley and C. G. Enke, *J. Electrochem. Soc.*, **112**, 947 (1965).
43. K. C. Liu and M. A. Anderson, *J. Electrochem. Soc.*, **143**, 124 (1996).
44. T. Pajkossy and D. M. Kolb, *Electrochim. Acta*, **46**, 3063 (2001).
45. P. S. Germain, W. G. Pell, and B. E. Conway, *Electrochim. Acta*, **49**, 1775 (2004).
46. T. Pajkossy and D. M. Kolb, *Electrochem. Commun.*, **9**, 1171 (2007).
47. R. P. Seward and E. C. Vieira, *J. Phys. Chem.*, **62**, 127 (1957).
48. M. M. Besli, A. K. Shukla, C. Wei, M. Metzger, J. Alvarado, J. Boell, D. Nordlund, G. Schneider, S. Hellstrom, C. Johnston, J. Christensen, M. M. Doeff, Y. Liu, and S. Kuppan, *J. Mater. Chem.*, **7**, 12593 (2019).
49. P. Yan, J. Zheng, M. Gu, J. Xiao, J. G. Zhang, and C. M. Wang, *Nat. Commun.*, **8**, 14101 (2017).
50. H. Zhang, F. Omenya, P. Yan, L. Luo, M. S. Whittingham, C. Wang, and G. Zhou, *ACS Energy Lett.*, **2**, 2607 (2017).
51. K. Edström, T. Gustafsson, and J. O. Thomas, *Electrochim. Acta*, **50**, 397 (2004).
52. D. Pritzl, T. Teufl, A. T. S. Freiberg, B. Strehle, J. Sicklinger, H. Sommer, P. Hartmann, and H. A. Gasteiger, *J. Electrochem. Soc.*, **166**, A4056 (2019).
53. C. Xu, K. Märker, J. Lee, A. Mahadevegowda, P. J. Reeves, S. J. Day, M. F. Groh, S. P. Emge, C. Ducati, B. L. Mehdi, C. C. Tang, and C. P. Grey, *Nat. Mater.*, **20**, 84 (2021).
54. Y.-K. Sun, S.-T. Myung, B.-C. Park, J. Prakash, I. Belharouak, and K. Amine, *Nat. Mater.*, **8**, 320 (2009).
55. Z. Sun, D. Wang, Y. Fan, L. Jiao, F. Li, T. Wu, D. Han, and L. Niu, *RSC Adv.*, **6**, 103747 (2016).
56. S. Ahmed, A. Pokle, S. Schweidler, A. Beyer, M. Bianchini, F. Walther, A. Mazilkin, P. Hartmann, T. Brezesinski, J. Janek, and K. Volz, *ACS Nano*, **13**, 10694 (2019).
57. F. Zhang, S. Lou, S. Li, Z. Yu, Q. Liu, A. Dai, C. Cao, M. F. Toney, M. Ge, X. Xiao, W.-K. Lee, Y. Yao, J. Deng, T. Liu, Y. Tang, G. Yin, J. Lu, D. Su, and J. Wang, *Nat. Commun.*, **11**, 3050 (2020).
58. P. Teichert, H. Jahnke, and E. Figgemeier, *J. Electrochem. Soc.*, **168**, 090532 (2021).
59. R. Ruess, S. Schweidler, H. Hemmelmann, G. Conforto, A. Bielefeld, D. A. Weber, J. Sann, M. T. Elm, and J. Janek, *J. Electrochem. Soc.*, **167**, 100532 (2020).
60. S. Schweidler, L. De Biasi, G. Garcia, A. Mazilkin, P. Hartmann, T. Brezesinski, and J. Janek, *ACS Appl. Energy Mater.*, **2**, 7375 (2019).
61. M. Bianchini, M. Roca-Ayats, P. Hartmann, T. Brezesinski, and J. Janek, *Angew. Chemie - Int. Ed.*, **58**, 10434 (2019).
62. M. A. Peck and M. A. Langell, *Chem. Mater.*, **24**, 4483 (2012).
63. F. Fiévet, P. Germi, F. de Bergevin, and M. Figlarz, *J. Appl. Crystallogr.*, **12**, 387 (1979).
64. J. H. Kim, S. J. Kim, T. Yuk, J. Kim, C. S. Yoon, and Y.-K. Sun, *ACS Energy Lett.*, **3**, 3002 (2018).
65. C. Tian, Y. Xu, D. Nordlund, F. Lin, J. Liu, Z. Sun, Y. Liu, and M. Doeff, *Joule*, **2**, 464 (2018).
66. J. A. Gilbert, I. A. Shkrob, and D. P. Abraham, *J. Electrochem. Soc.*, **164**, A389 (2017).
67. S. M. Bak, E. Hu, Y. Zhou, X. Yu, S. D. Senanayake, S. J. Cho, K. B. Kim, K. Y. Chung, X. Q. Yang, and K. W. Nam, *ACS Appl. Mater. Interfaces*, **6**, 22594 (2014).
68. J. Sicklinger, M. Metzger, H. Beyer, D. Pritzl, and H. A. Gasteiger, *J. Electrochem. Soc.*, **166**, A2322 (2019).
69. R. Jung, R. Morasch, P. Karayaylali, K. Phillips, F. Maglia, C. Stinner, Y. Shao-Horn, and H. A. Gasteiger, *J. Electrochem. Soc.*, **165**, A132 (2018).